nature materials

ARTICLES

https://doi.org/10.1038/s41563-022-01294-2

Directed cell migration towards softer environments

Aleksi Isomursu[1,12], Keun-Young Park[2,12], Jay Hou[3,12], Bo Cheng[4,5,12], Mathilde Mathieu[1], Ghaidan A. Shamsan[3], Benjamin Fuller[3], Jesse Kasim[3], M. Mohsen Mahmoodi[2], Tian Jian Lu[6,7], Guy M. Genin[4,5,8], Feng Xu[4,5], Min Lin[4,5] ✉, Mark D. Distefano[2] ✉, Johanna Ivaska[1,9,10,11] ✉ and David J. Odde[3] ✉

How cells sense tissue stiffness to guide cell migration is a fundamental question in development, fibrosis and cancer. Although durotaxis—cell migration towards increasing substrate stiffness—is well established, it remains unknown whether individual cells can migrate towards softer environments. Here, using microfabricated stiffness gradients, we describe the directed migration of U-251MG glioma cells towards less stiff regions. This 'negative durotaxis' does not coincide with changes in canonical mechanosensitive signalling or actomyosin contractility. Instead, as predicted by the motor–clutch-based model, migration occurs towards areas of 'optimal stiffness', where cells can generate maximal traction. In agreement with this model, negative durotaxis is selectively disrupted and even reversed by the partial inhibition of actomyosin contractility. Conversely, positive durotaxis can be switched to negative by lowering the optimal stiffness by the downregulation of talin—a key clutch component. Our results identify the molecular mechanism driving context-dependent positive or negative durotaxis, determined by a cell's contractile and adhesive machinery.

The capacity of living cells to undergo controlled migration is critical for tissue homeostasis and development, and underlies pathological conditions like cancer metastasis[1,2]. Cells migrate in response to chemical and physical cues including the elasticity, or stiffness, of the surrounding extracellular matrix (ECM). The well-known tendency for many cells to migrate towards stiffer substrates, known as durotaxis[3–8], has implications for both developmental morphogenesis[9,10] and cancer cell invasion[8,11,12].

Despite progress in empirically identifying environmental conditions and molecular components that enable or promote durotaxis[4,5,13–15], our understanding of its fundamental mechanisms in different cell types is lacking. A long-standing mathematical model for cell migration is based on the motor–clutch mechanism[16–19], in which F-actin filaments polymerize against the plasma membrane to push the cell edge forward while being simultaneously pulled away from the cell edge by adenosine triphosphate (ATP)-dependent myosin II ('molecular motors') and pushed by force from the ATP-dependent polymerization itself. Retrograde F-actin flow can be mitigated by mechanical connections or 'clutches', typically integrin-mediated adhesions, between the F-actin and ECM to generate traction and bias cell movement towards more adhesive environments[20,21]. These traction forces are critical for cell migration; as a result, they have also been linked to durotaxis. For example, fibroblasts on stiffness gradients exhibit asymmetric traction that has been postulated to directly contribute to their polarization and migration up the gradient[6,22]. Recently, differences in intracellular contractility and adhesivity to the ECM have been proposed to explain why some cells are more prone to durotax than others[12]. Interactions between actomyosin machinery and integrin-mediated adhesions have also been implicated in neuronal growth and mechanosensitive pathfinding[23–25]. However, the unifying principles underlying these behaviours across cell types have not been established.

Recently, cellular traction forces were shown to be maximal on substrates of an 'optimal stiffness' that can be predicted by the motor–clutch model[18,19,26–30]. However, the biological relevance of this on cell behaviour remains to be fully elucidated. Due to the key role of traction in driving mesenchymal cell migration, we predicted that any cell whose adhesion dynamics are governed by the motor–clutch model could potentially migrate towards softer environments, if such environments were closer to the cell's optimal stiffness for maximal traction generation. We call this behaviour 'negative durotaxis'.

U-251MG glioblastoma cells undergo negative durotaxis

To test our hypothesis, we seeded U-251MG human glioblastoma cells, previously shown to exhibit maximal traction at an optimal stiffness of 5–10 kPa (Fig. 1a)[29], on fibronectin-functionalized polyacrylamide hydrogels having a continuous stiffness gradient of approximately 0.5–22.0 kPa (Supplementary Fig. 1a,b)[31]—a range

[1]Turku Bioscience Centre, University of Turku and Åbo Akademi University, Turku, Finland. [2]Department of Chemistry, University of Minnesota, Minneapolis, MN, USA. [3]Department of Biomedical Engineering, University of Minnesota, Minneapolis, MN, USA. [4]The Key Laboratory of Biomedical Information Engineering of Ministry of Education, School of Life Science and Technology, Xi'an Jiaotong University, Xi'an, People's Republic of China. [5]Bioinspired Engineering and Biomechanics Center (BEBC), Xi'an Jiaotong University, Xi'an, People's Republic of China. [6]State Key Laboratory of Mechanics and Control of Mechanical Structures, Nanjing University of Aeronautics and Astronautics, Nanjing, People's Republic of China. [7]MOE Key Laboratory of Multifunctional Materials and Structures, Xi'an Jiaotong University, Xi'an, People's Republic of China. [8]NSF Science and Technology Center for Engineering Mechanobiology, Washington University in St. Louis, St. Louis, MO, USA. [9]Department of Life Technologies, University of Turku, Turku, Finland. [10]InFLAMES Research Flagship Center, University of Turku, Turku, Finland. [11]Foundation for the Finnish Cancer Institute, Helsinki, Finland. [12]These authors contributed equally: Aleksi Isomursu, Keun-Young Park, Jay Hou, Bo Cheng. ✉e-mail: minlin@xjtu.edu.cn; diste001@umn.edu; johanna.ivaska@utu.fi; oddex002@umn.edu

representative of healthy and malignant brain tissue[32]. We observed a strong tendency for these cells to undergo negative durotaxis, migrating from the stiffest areas to regions of intermediate stiffness over time (Fig. 1b,c). Fewer cells were observed in the softest regions, implying that cells below the optimal stiffness underwent conventional positive durotaxis. To exclude cell proliferation as a cause of these differences, we quantified the rate of 5-ethynyl-2′-deoxyuridine (EdU) incorporation in cells cultured on homogeneous 0.5, 9.6 and 60.0 kPa substrates. Proliferation was equal on the 9.6 and 60.0 kPa hydrogels and only slightly lower on the 0.5 kPa substrates (Supplementary Fig. 2a,b), suggesting that the absence of cells in the stiffer regions of the gradient was indeed due to biased migration. This was further validated by live-cell tracking of cells on stiffness gradients. The cells initially located in areas below the optimal stiffness (<10 kPa) exhibited movement towards increasingly stiff regions, whereas cells residing in areas above the stiffness optimum (>10 kPa) displayed a significant tendency to migrate towards the softer regions (Fig. 1d and Supplementary Fig. 3a,b).

As an additional demonstration of negative durotaxis, we cultured U-251MG cells on photoresponsive hydrogels with alternating 8 and 15 kPa regions, connected by steep stiffness gradients (Fig. 1e, Supplementary Figs. 4a,b and 5a–d, and Supplementary Note 1). Here 20-μm-wide fibronectin lines were printed across the gradients to facilitate cell motility. Live-cell imaging revealed that cells migrated along the fibronectin lines and preferentially clustered in the softer 8 kPa regions (Fig. 1f,g, Supplementary Fig. 3c,d and Supplementary Video 1). Moreover, tracking of individual U-251MGs confirmed that any cell making contact with a stiffness gradient preferentially migrated to the softer 8 kPa side (Fig. 1h, Supplementary Fig. 3e and Supplementary Video 2). Finally, we confirmed that biased migration on either type of stiffness gradient was not due to differences in fibronectin density, that is, haptotaxis, as ligand distribution appeared uniform in both experimental models (Supplementary Figs. 1c and 5e–f). Taken together, these data demonstrate that U-251MGs are capable of negative durotaxis from stiff to soft environments, consistent with their stiffness optimum for maximal traction.

Negative durotaxis does not correlate with mechanosignalling

To gain an insight into the molecular basis of negative durotaxis, we investigated the key mediators of mechanotransduction, whereby biomechanical cues are translated into changes in cell signalling and behaviour[33]. We speculated that a biphasic response in any of these could, in part, modulate the negative durotaxis of U-251MGs. However, no changes were observed in myosin II light chain (MLC2), focal adhesion kinase (FAK) or extracellular signal-regulated kinase (ERK) phosphorylation in U-251MGs cultured on substrates with moduli of 0.5, 8.0 or 50.0 kPa (Fig. 2a,b). These results were surprising because in most adherent cell types, increasing the substrate stiffness supports integrin clustering and focal adhesion (FA) growth, promoting the activation of mechanosensitive downstream signalling pathways[19,34,35].

This prompted us to compare FAs in U-251MGs, capable of negative durotaxis, and MDA-MB-231 breast adenocarcinoma cells, which reportedly undergo positive durotaxis[8]. As expected, MDA-MB-231s displayed stiffness-induced growth of paxillin-positive FAs (Supplementary Fig. 6a), whereas U-251MGs displayed very few FAs even on 60 kPa substrates, as confirmed by the immunostaining of paxillin (Fig. 2c) and additional FA markers, namely, vinculin and phosphorylated FAK (Supplementary Fig. 6b). This was not due to the low expression of mechanosensitive adhesion proteins talin-1, talin-2 or vinculin, or due to low myosin II activity (p-MLC2), as these were expressed at comparable levels in U-251MG, MDA-MB-231 and human osteosarcoma U-2 OS—another FA-forming cell line[36] (Supplementary Figs. 6c,d and 16). Nevertheless, U-251MGs displayed high β1-integrin activity and their spreading on fibronectin was sensitive to β1-integrin inhibition with a function-blocking antibody (Mab13) (Supplementary Fig. 6e–g), suggesting that they interact with their substrate primarily through integrins.

Hippo-family proteins yes-associated protein 1 (YAP) and transcriptional co-activator with PDZ-binding motif (TAZ) are transcriptional co-regulators that integrate cues from different mechanical and biochemical sources to direct cell behaviour. Nuclear localization and activation of YAP/TAZ on stiff substrates are linked to increased F-actin assembly and FA formation; conversely, YAP/TAZ can promote adhesion turnover and cell migration[37] and baseline YAP activity may even be necessary for conventional durotaxis[14]. We stained endogenous YAP from MDA-MB-231s and observed robust stiffness-induced nuclear translocation (Fig. 2d,e). In contrast, U-251MGs displayed much lower nuclear YAP on both soft and stiff substrates, with a slight increase but no visible peak between 0.5 and 60.0 kPa (Fig. 2d,e). Thus, the mechanosensitive signalling responses of U-251MGs are minimal and not specific to the 5–10 kPa range, and cannot explain negative durotaxis.

Negative durotaxis can be explained by motor–clutch dynamics

The optimal stiffness for U-251MG traction and the increasing overall motility of these cells (random motility coefficient (RMC)) with stiffness up to 100 kPa can be explained by motor–clutch dynamics[29]. Without talin unfolding and vinculin-mediated 'clutch reinforcement' and FA growth, the motor–clutch model naturally predicts a biphasic dependence of traction forces on substrate stiffness[19]. After confirming that U-251MGs preferentially migrated towards their known stiffness optimum in all our experimental conditions (Fig. 1a–h), we investigated whether the stochastic computational

Fig. 1 | U-251MG glioblastoma cells undergo negative durotaxis. a, Schematic of U-251MG traction, maximal on 5–10 kPa substrates[29], and how it relates to the two stiffness gradients employed here. **b**, Representative region of a diffusion-based polyacrylamide stiffness gradient (Young's modulus, ~0.5–22.0 kPa) at the outset of the experiment and 48 h later (top). U-251MG cells are indicated by nuclear staining. Scale bar, 500 μm. Quantification of cells across the gradient (bottom). **c**, Cell density in different parts of the stiffness gradient. The bins denote pooled regions of interest (ROIs) in the bottom-, middle- and top-third of the gradient. Mean ± standard error of the mean (s.e.m.) of $n = 36$ (day zero, low), 22 (day zero, intermediate), 14 (day zero, high), 42 (day two, low), 16 (day two, intermediate) and 14 (day two, high) ROIs, analysed by the Kruskal–Wallis one-way analysis of variance (ANOVA) and Dunn's post hoc test. **d**, Angular displacements and forward migration indices (FMIs) of individual U-251MG cells migrating in the softer (<10 kPa, left) and stiffer (>10 kPa, right) regions of a 0.5–22.0 kPa gradient. Here $n = 174$ (>10 kPa) and 264 (<10 kPa) cells from three independent experiments. Analysed by the Wilcoxon signed-rank test (two sided). **e**, Schematic of photoresponsive hydrogels with steep repeating stiffness gradients. **f**,**g**, U-251MG migration on photoresponsive gradient hydrogels. A representative example (**f**) and quantification (**g**) of the change in cell density across the gradients over time. The blue overlay denotes softer, UV-exposed regions. The vertical and horizontal grey lines in **f** are out-of-focus markings on the underlying glass, used as a reference. Scale bar, 200 μm. Mean ± 95% confidence interval (CI) from $n = 24$ fields of view, from two independent experiments. **h**, Violin plots of accumulated distance migrated by individual cells along the x axis over 12 h, starting from a gradient (top) or from the middle of a compliant region (bottom). The vertical lines denote medians, $n = 164$ (centred) and 296 (interface) cells from two independent experiments. Analysed by a sign test (two sided).

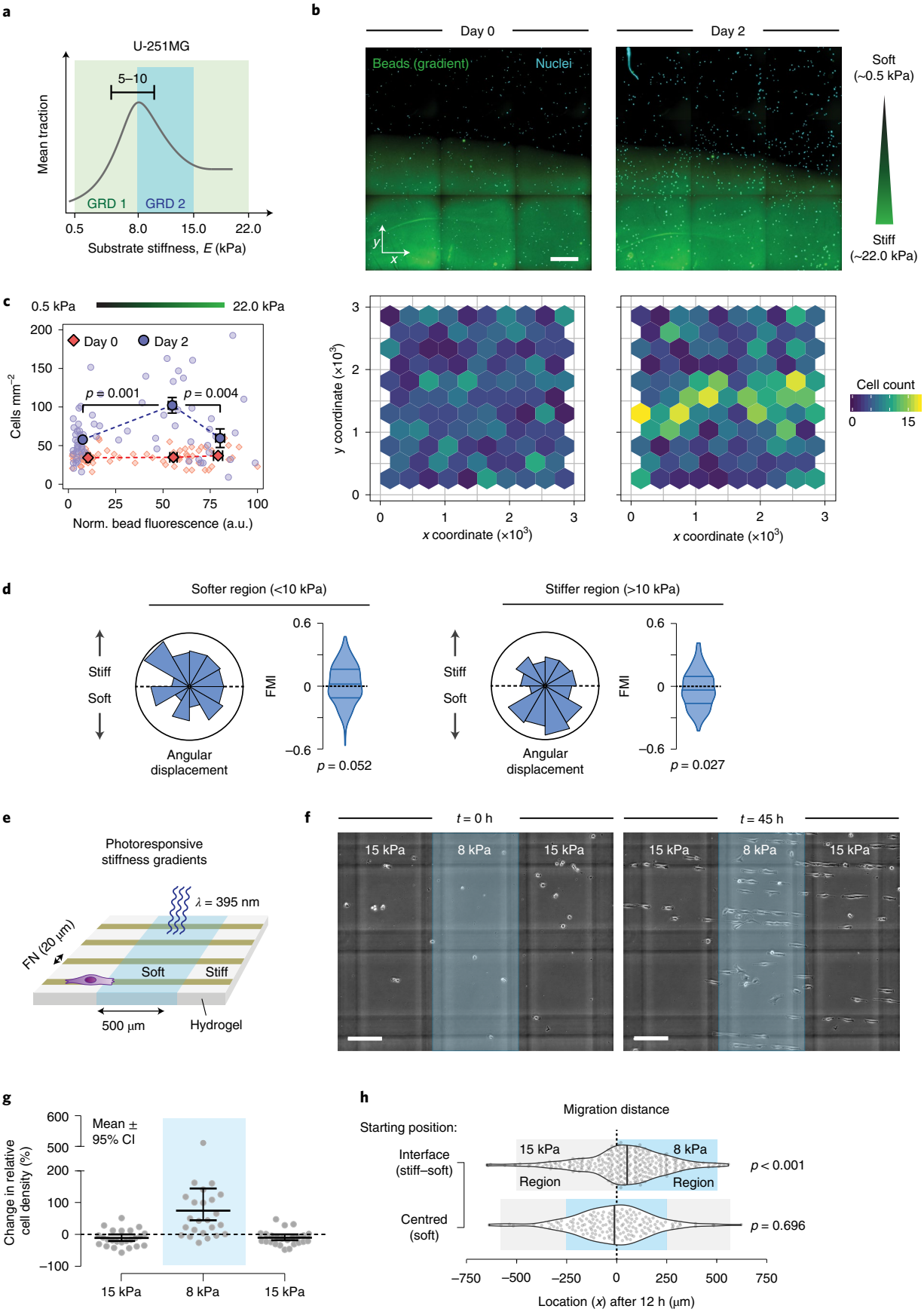
a
U-251MG
5–10
Mean traction
GRD 1
GRD 2
0.5
8.0
15.0
22.0
Substrate stiffness, E (kPa)
b
Day 0
Day 2
Beads (gradient)
Nuclei
Soft
(~0.5 kPa)
Stiff
(~22.0 kPa)
c
0.5 kPa
22.0 kPa
Day 0
Day 2
p = 0.001
p = 0.004
Cells mm−2
Norm. bead fluorescence (a.u.)
y coordinate (×10³)
x coordinate (×10³)
Cell count
0
15
d
Softer region (<10 kPa)
Stiffer region (>10 kPa)
Stiff
Soft
Angular displacement
FMI
p = 0.052
p = 0.027
e
Photoresponsive stiffness gradients
λ = 395 nm
FN (20 μm)
Soft
Stiff
500 μm
Hydrogel
f
t = 0 h
t = 45 h
15 kPa
8 kPa
15 kPa
g
Mean ± 95% CI
Change in relative cell density (%)
15 kPa
8 kPa
15 kPa
h
Migration distance
Starting position:
Interface (stiff–soft)
Centred (soft)
15 kPa
8 kPa
Region
Region
p < 0.001
p = 0.696
Location (x) after 12 h (μm)

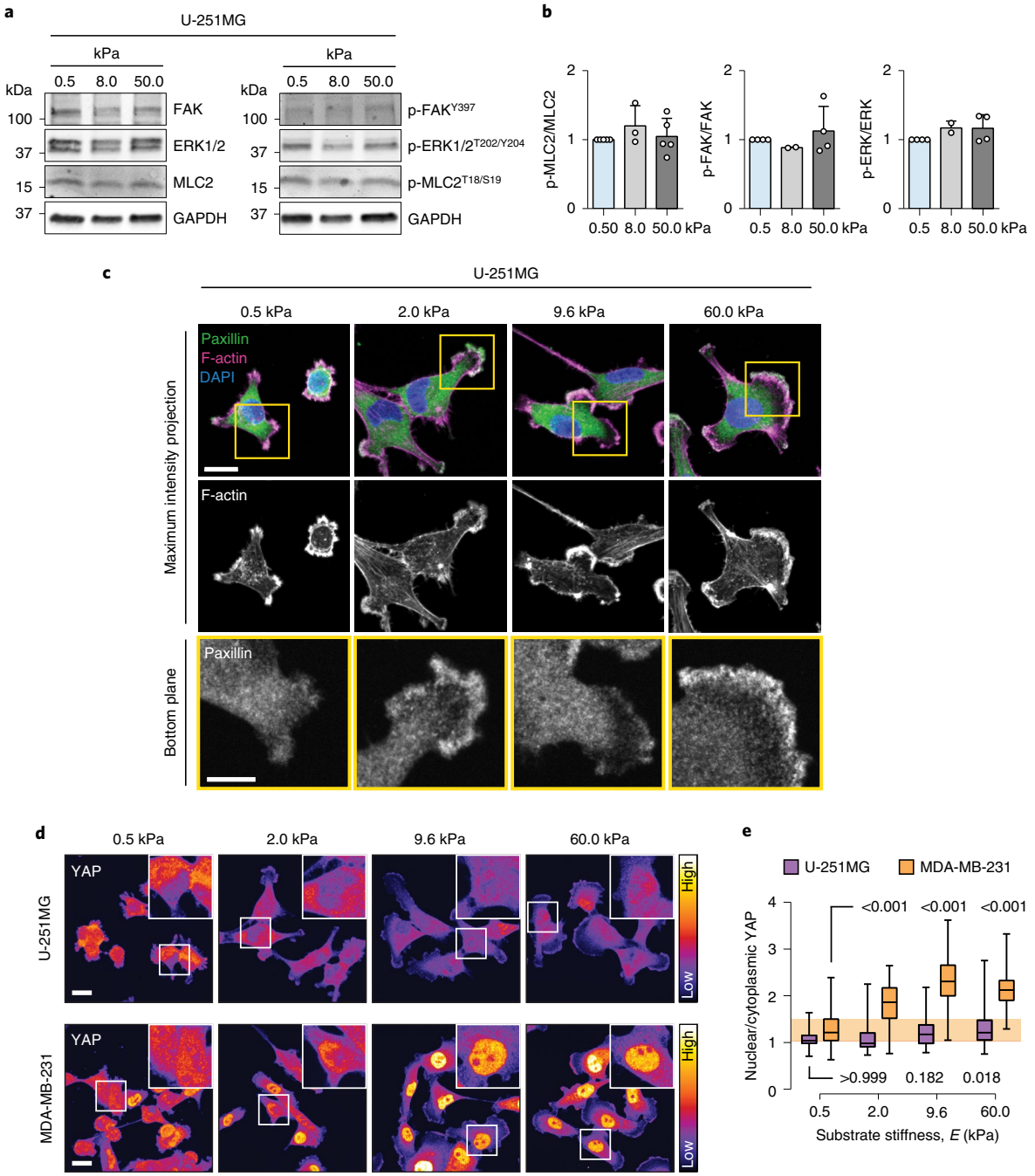

Fig. 2 | U-251MG cells display limited mechanosensitive signalling and adhesion maturation. a,**b**, Representative western blot (**a**) and quantification (**b**) depicting protein phosphorylation in U-251MGs on 0.5–50.0 kPa substrates. Mean ± standard deviation (s.d.) of $n = 5$ (p-MLC2, 0.5 kPa), 3 (p-MLC2, 8.0 kPa), 5 (p-MLC2, 50.0 kPa), 4 (p-FAK, 0.5 kPa), 2 (p-FAK, 8.0 kPa), 4 (p-FAK, 50.0 kPa), 4 (p-ERK, 0.5 kPa), 2 (p-ERK, 8.0 kPa) and 4 (p-ERK, 50.0 kPa) independent experiments. **c**, Immunofluorescence images of paxillin and F-actin in U-251MGs on 0.5–60.0 kPa substrates. Individual focal planes from confocal stacks corresponding to the basal side of each cell (bottom). Scale bars, 20 μm (main) and 10 μm (ROI). Representative of three independent experiments. **d**,**e**, Immunofluorescence images (**d**) and quantification (**e**) showing the intracellular localization of YAP as a function of substrate stiffness in U-251MG and MDA-MB-231 cells. The insets depict the representative nuclei. Scale bar, 20 μm. Each box displays the upper and lower quartiles and a median and the whiskers denote the minimum and maximum values. Here $n = 65$ (U-251MG, 0.5 kPa), 57 (U-251MG, 2.0 kPa), 96 (U-251MG, 9.6 kPa), 85 (U-251MG, 60.0 kPa), 135 (MDA-MB-231, 0.5 kPa), 73 (MDA-MB-231, 2.0 kPa), 89 (MDA-MB-231, 9.6 kPa) and 85 (MDA-MB-231, 60.0 kPa) cells. Analysed by the Kruskal–Wallis one-way ANOVA and Dunn's post hoc test; p values are indicated in the figure.

simulation of cell-level motor–clutch dynamics would be sufficient to reproduce negative durotaxis (Fig. 3a and Supplementary Note 2). We simulated the migration of individual U-251MGs on mechanically homogeneous substrates for one hour to allow the system to reach a dynamic steady state and then placed each cell on a continuous substrate consisting of alternating 60-μm-wide regions of low and high stiffness, joined together by continuous 30-μm-wide stiffness gradients (Fig. 3b and Supplementary Fig. 7).

On 10–100 pN nm^{-1} gradients, corresponding to ~10–100 kPa for typical adhesion sizes[38], and where the cells' optimal stiffness

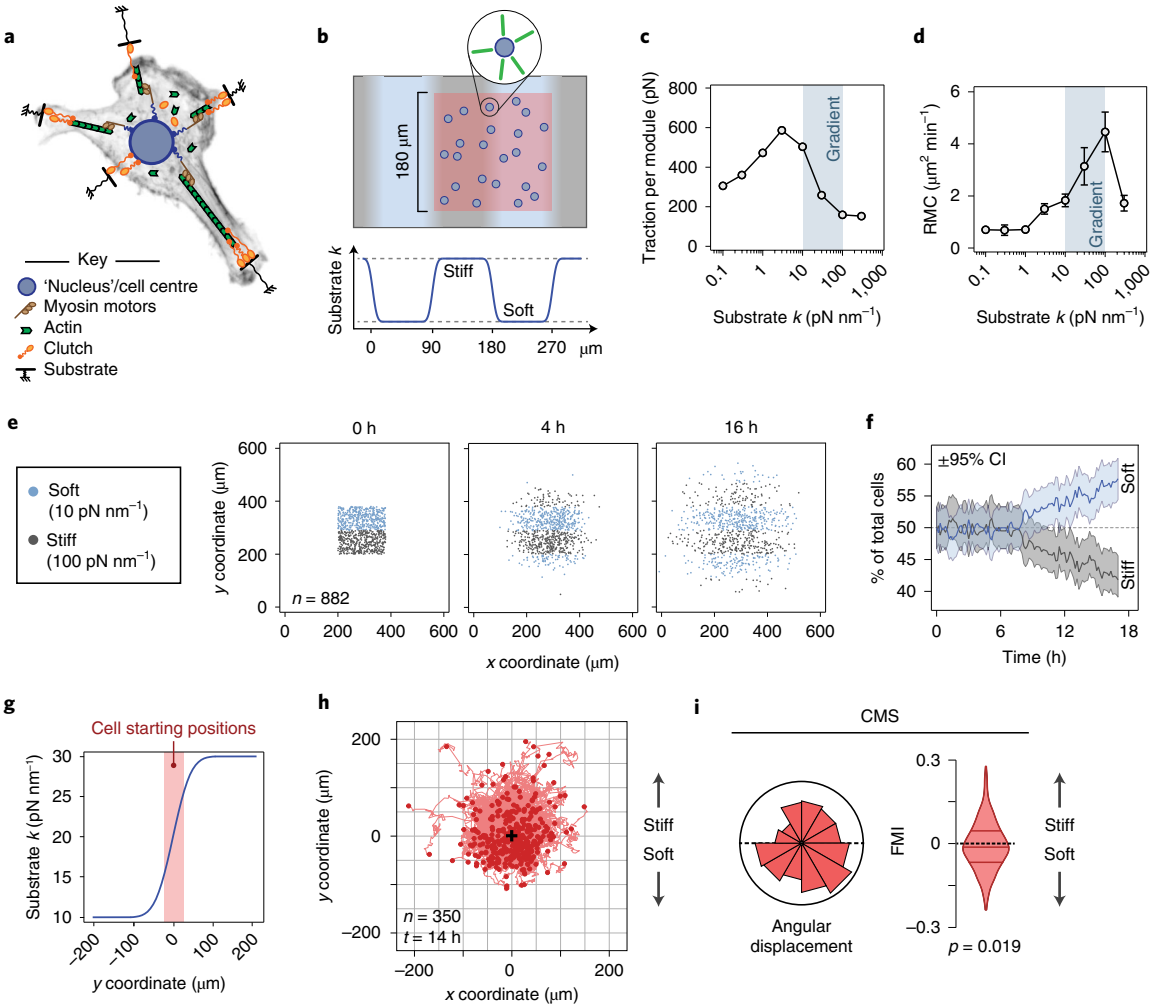

Fig. 3 | Motor-clutch simulations recapitulate negative durotaxis. a, Schematic of the cell migration simulator[29]. Individual modules and a central cell body are attached to the elastic substrate by sets of clutch molecules. **b**, Experimental setup used here and in Supplementary Figs. 8 and 9. The simulated cells in a dynamic steady state were placed on a substrate with repeating stiff and soft regions and tracked over time. An equal number of cells were placed on both stiffnesses (red area). **c**,**d**, Module-wise traction forces (**c**) and RMC (**d**) of the simulated cells as a function of substrate stiffness. The overlays highlight the range of the 10–100 pN nm^{-1} gradient in **e** and **f**. Mean ± s.e.m. of $n = 10$ cells. **e**,**f**, Evolution of cell density on mechanically heterogeneous substrates over time. Coordinates of individual cells 0, 4 and 16 h into the simulation (**e**). Stiff (≥55 pN nm^{-1}) and compliant (<55 pN nm^{-1}) regions are indicated by grey and blue, respectively. Fraction of cells residing in the stiff and soft regions over the course of the simulation (**f**). ±95% CI, $n = 882$ cells. **g**, Experimental setup used for investigating the migration tracks of individual simulated cells on a continuous stiffness gradient. Cells in a dynamic steady state were randomly placed on the linear part of a 10–30 pN nm^{-1} gradient and tracked for 14 in-simulation hours. **h**, Tracks from individual cells on the 10–30 pN nm^{-1} gradient. The origin (0,0) is highlighted by a black '+'; $n = 350$ cells. **i**, Angular displacements and forward migration indices of the cells depicted in **h**. Analysed by the Wilcoxon signed-rank test (two sided).

overlaps with the softer regions (Fig. 3c,d), we found that the majority of cells translocated away from stiffer areas in the first 12 h of the simulation (Fig. 3e,f). This occurred despite the cells being less motile (that is, having lower RMC) on the softer substrate (Fig. 3d). On stiffness gradients, cellular protrusions (modules) displayed higher average traction on soft rather than on stiff regions (Supplementary Fig. 8a–c), and cells also preferentially turned towards the softer areas (Supplementary Fig. 8d). By altering the range of the gradient, such that the side associated with higher predicted traction was the stiffer one, durotaxis could be reversed and cells primarily clustered in the stiff regions (Supplementary Fig. 9). Finally, we replaced the repeating graded substrates with a continuous 10–30 pN nm^{-1} stiffness gradient to study the tracks of individual cells in quantitative detail. Each cell was randomly placed on the linear region of the gradient (Fig. 3g) and tracked for 14 in-simulation hours (Fig. 3h). We confirmed that the majority of cells migrated towards the softer substrate, recapitulating the behaviour observed in U-251MGs in vitro (Fig. 3i).

We verified the generality of these principles by applying them to model axonal pathfinding in neuronal development and regeneration (Supplementary Figs. 10 and 11 and Supplementary Note 3). The tendency for *Xenopus* retinal ganglion cell axons to grow towards softer tissue, while possibly confounded by complex in vivo factors that correlate with stiffness—including collective effects based on differential axon growth rates—is still potentially analogous to the whole-cell negative durotaxis that we report[24]. Neurite elongation and pathfinding via the actin-rich neuronal growth cone (GC) at the distal end of the axon involves the contractile filopodia of variable length and orientation (Supplementary Fig. 10a). Applying our model to individual filopodia (Supplementary Fig. 10b) as well as GCs with multiple filopodia (Supplementary Fig. 11a), we found that the protrusions elongated faster and generated more traction

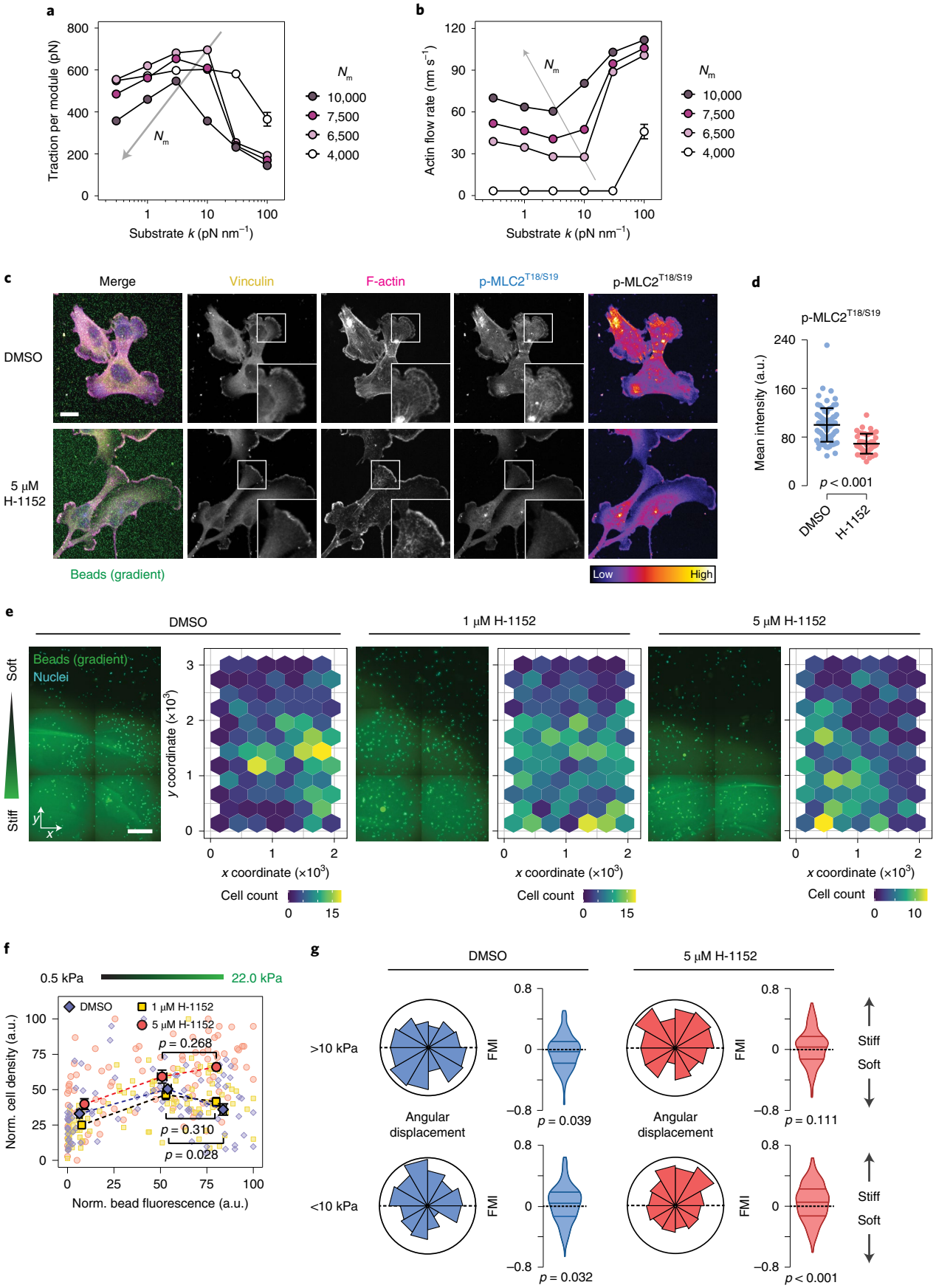
a
Traction per module (pN)
800
600
400
200
0
1
10
100
Substrate k (pN nm−1)
Nm
10,000
7,500
6,500
4,000
b
Actin flow rate (nm s−1)
120
90
60
30
0
1
10
100
Substrate k (pN nm−1)
Nm
10,000
7,500
6,500
4,000
c
Merge
Vinculin
F-actin
p-MLC2T18/S19
p-MLC2T18/S19
DMSO
5 μM H-1152
Beads (gradient)
Low
High
d
p-MLC2T18/S19
Mean intensity (a.u.)
240
160
80
0
p < 0.001
DMSO
H-1152
e
DMSO
1 μM H-1152
5 μM H-1152
Soft
Stiff
Beads (gradient)
Nuclei
y
x
y coordinate (×10³)
x coordinate (×10³)
Cell count
0
15
10
f
0.5 kPa
22.0 kPa
DMSO
1 μM H-1152
5 μM H-1152
p = 0.268
p = 0.310
p = 0.028
Norm. cell density (a.u.)
Norm. bead fluorescence (a.u.)
g
DMSO
5 μM H-1152
>10 kPa
<10 kPa
Angular displacement
FMI
p = 0.039
p = 0.111
p = 0.032
p < 0.001
Stiff
Soft

Fig. 4 | Decreasing actomyosin contractility selectively inhibits negative durotaxis in U-251MG cells. a,**b**, Simulated traction forces (**a**) and actin retrograde flow rates (**b**) as a function of substrate stiffness for different pools of molecular motors. The grey arrows denote shifts in the local minima/maxima on increasing motor numbers. Mean ± s.e.m. of $n = 10$ cells. **c**,**d**, Immunofluorescence images (**c**) and quantification (**d**) depicting vinculin and levels of phosphorylated MLC2 in U-251MG cells after 48 h on 0.5–22.0 kPa gradients, with or without the ROCK inhibitor H-1152. Scale bar, 20 μm. Mean ± s.d. of $n = 83$ (DMSO) and 42 (H-1152) cells, analysed by the Mann–Whitney test (two sided). Representative of two independent experiments. **e**, Representative regions of three 0.5–22.0 kPa stiffness gradients, 48 h after being seeded with U-251MG cells and supplemented with varying concentrations of H-1152. Scale bar, 500 μm. Interspaced with depictions of cell counts across the gradients. **f**, Relative cell densities in different parts of the gradients, overlaid with the binned data. Mean ± s.e.m. of $n = 35$ (DMSO, low), 22 (DMSO, intermediate), 27 (DMSO, high), 39 (1 μM H-1152, low), 26 (1 μM H-1152, intermediate), 31 (1 μM H-1152, high), 39 (5 μM H-1152, low), 16 (5 μM H-1152, intermediate) and 41 (5 μM H-1152, high) ROIs per bin, from two gradient hydrogels per condition, representative of two independent experiments. Analysed by the Mann–Whitney test (two sided). **g**, Angular displacements and forward migration indices of individual U-251MG cells migrating in the stiffer (>10 kPa, top) and softer (<10 kPa, bottom) regions of 0.5–22.0 kPa gradients. $n = 204$ (DMSO, >10 kPa), 238 (DMSO, <10 kPa), 177 (H-1152, >10 kPa) and 327 (H-1152, <10 kPa) cells from one (DMSO) to two (H-1152) independent experiments. Analysed by the Wilcoxon signed-rank test (two sided).

on soft substrates (0.01–0.10 pN nm^{-1}) (Supplementary Figs. 10c–h and 11b). This was consistent both with earlier predictions of relatively low optimal stiffness for neurons[18,39,40] and with our hypothesis that positive and negative durotaxis are governed by motor–clutch dynamics in concert with optimal stiffness. The results also suggested that gradient strength may further increase the propensity for negative durotaxis: GCs steered to more compliant regions on substrates with stronger gradients (reaching a maximum at ~10 pN nm^{-1}/20 μm), but did not change direction on mild gradients (~0.1 pN nm^{-1}/20 μm) or on substrates that were stiff overall compared with the optimum case (>1 pN nm^{-1}) (Supplementary Fig. 11c–e).

Inhibiting myosin contractility restricts negative durotaxis

The motor–clutch model of cell migration states that a cell's capacity to respond to substrate mechanics is intrinsically linked to its pool of available molecular motors, or actomyosin contractility, such that the partial inhibition of intracellular contractility would be expected to shift the cell's stiffness optimum up slightly[27]. We confirmed this using our cell migration simulator (CMS) model and observed a threefold increase in the optimal substrate stiffness when motor numbers were gradually decreased, before the system stalled, stopping actin dynamics and cell migration on all but the stiffest substrates (Fig. 4a,b).

We sought to experimentally validate these observations by treating U-251MG cells with intermediate (1 μM) and high (5 μM) concentrations of Rho-associated kinase (ROCK) 1/2 inhibitor H-1152. Higher concentrations of the inhibitor significantly reduced intracellular contractility (MLC2 phosphorylation) and increased the formation of actin-enriched ruffles at the cell periphery, whereas mature vinculin-positive adhesions remained undetectable, similar to the control cells (Fig. 4c,d and Supplementary Fig. 12a). Importantly, H-1152 suppressed the characteristic negative durotaxis of U-251MGs and promoted localization to the stiffer regions of the 0.5–22.0 kPa gradients over time, in a dose-dependent manner (Fig. 4e,f). Live-cell imaging of the control and H-1152-treated U-251MGs further confirmed a shift in the durotaxis: although control cells initially located in stiffer areas (>10 kPa) migrated significantly more towards softer-substrate regions, the ROCK-inhibitor-treated cells lost their negative durotaxis and instead displayed a trend of positive durotaxis, with trajectories mainly towards stiffer substrates (Fig. 4g, Supplementary Fig. 12b and Supplementary Video 3). A similar effect was detected when U-251MGs were treated with intermediate concentrations (5 μM) of myosin II inhibitor blebbistatin, whereas higher concentrations (25 μM) inhibited durotaxis (and possibly migration) altogether (Supplementary Fig. 12c,d). These modelling and experimental data indicate actomyosin contractility as a key determinant in tuning the cell durotactic behaviour.

Talin depletion can switch positive durotaxis to negative

Although U-251MGs and neurons exhibit biphasic traction forces in the physiological stiffness range, many adherent cell types do not[11,19,41,42]. Rather, their traction increases as a function of substrate stiffness unless talin- and vinculin-mediated FA formation is disrupted, for example, by the depletion of both talin isoforms[19] (Fig. 5a). Therefore, we hypothesized that targeting adhesion reinforcement can generate an intermediate stiffness optimum and enable negative durotaxis in cell types that normally undergo only positive durotaxis. To test this, we used short interfering RNAs (siRNAs) to reduce talin-1 and talin-2 expression in MDA-MB-231 cells that exert increasing traction with increasing substrate stiffness[42] and undergo

Fig. 5 | Lowering stiffness optimum by blocking adhesion reinforcement shifts cells from positive to negative durotaxis. a, Schematic of the relationship between traction forces, substrate stiffness and talin-/vinculin-mediated 'clutch reinforcement'. Depletion of these clutch components forces some cell types back into a biphasic traction regime[19]. **b**, Representative western blot depicting talin-1 and talin-2 double knockdown in MDA-MB-231 cells. The same siRNA oligos have been used in the subsequent panels. **c**,**d**, Immunofluorescence images (**c**) and quantification (**d**) of FAs in MDA-MB-231s on a 60 kPa substrate without and after talin knockdown. Scale bar, 20 μm. Mean ± s.d. of $n = 35$ (siCTRL) and 32 (siTLN1+2) cells, analysed by the Mann–Whitney test (two sided). **e**, Distribution of FA sizes in control and talin-low cells. Histograms overlaid with probability density functions; the dashed lines indicate medians. Here $n = 1{,}844$ (siCTRL) and 524 (siTLN1+2) adhesions from the 32–35 cells in **d**, analysed by the Kolmogorov–Smirnov (K-S) test (two sided). Representative of two independent experiments. **f**–**h**, Traction force analysis of control and talin-low MDA-MB-231s. Total force exerted by the cells as a function of substrate stiffness (**f**). Background, BG. Mean ± s.e.m. of $n = 23$ (siCTRL, 0.5 kPa), 22 (siCTRL, 2.0 kPa), 42 (siCTRL, 9.6 kPa), 55 (siCTRL, 22.0 kPa), 18 (siTLN1+2, 0.5 kPa), 27 (siTLN1+2, 2.0 kPa), 52 (siTLN1+2, 9.6 kPa) and 37 (siTLN1+2, 22.0 kPa) cells from three independent experiments. Traction maps from cells on 22 kPa substrate, representative of three independent experiments (**g**). The cell outlines are indicated by white dashed lines. Scale bar, 20 μm. **h**, Histograms of the 22 kPa data overlaid with probability density functions, with the dashed lines indicating medians. $n = 55$ (siCTRL) and 37 (siTLN1+2) cells from three independent experiments. Analysed by the Kolmogorov Smirnov test (two sided). **i**, Representative regions of two 0.5–22.0 kPa polyacrylamide stiffness gradients, 72 h after being seeded with MDA-MB-231 cells (indicated by nuclear staining) (left). Scale bar, 500 μm. Quantification of cells across the gradients (right). **j**, Relative cell densities in different parts of the gradients, overlaid with the binned data. Mean ± s.e.m. of $n = 13$ (siCTRL, low), 32 (siCTRL, intermediate), 74 (siCTRL, high), 49 (siTLN1+2, low), 141 (siTLN1+2, intermediate) and 38 (siTLN1+2, high) ROIs per bin, from one (siCTRL) or two (siTLN1+2) gradient gels, representative of three independent experiments. Analysed by the Mann–Whitney test (two sided).

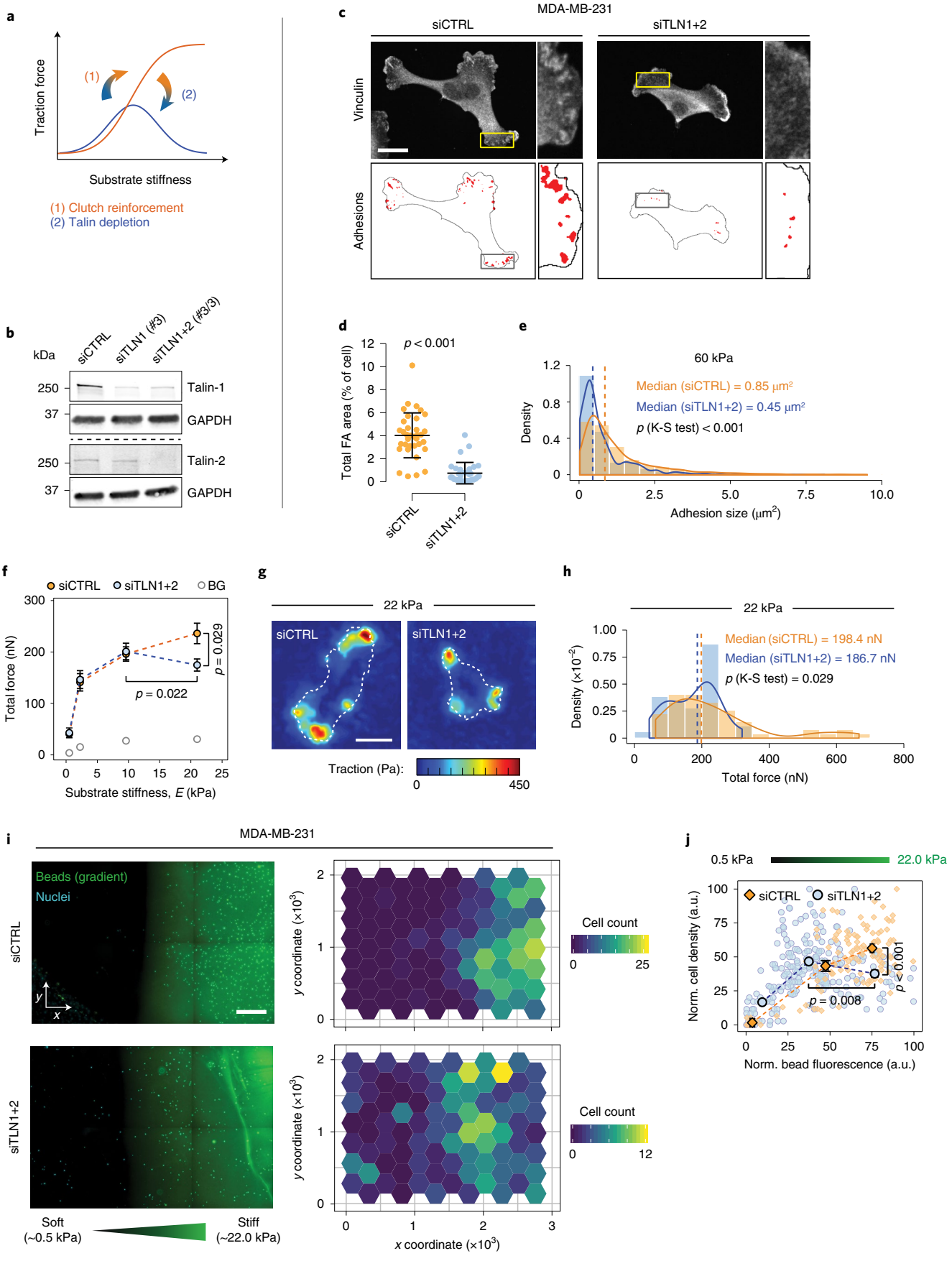
a
Traction force
(1)
(2)
Substrate stiffness
(1) Clutch reinforcement
(2) Talin depletion
b
kDa
siCTRL
siTLN1 (#3)
siTLN1+2 (#3/3)
250
Talin-1
37
GAPDH
250
Talin-2
37
GAPDH
c
MDA-MB-231
siCTRL
siTLN1+2
Vinculin
Adhesions
d
p < 0.001
Total FA area (% of cell)
siCTRL
siTLN1+2
e
60 kPa
Median (siCTRL) = 0.85 μm²
Median (siTLN1+2) = 0.45 μm²
p (K-S test) < 0.001
Density
Adhesion size (μm²)
f
siCTRL
siTLN1+2
BG
Total force (nN)
p = 0.029
p = 0.022
Substrate stiffness, E (kPa)
g
22 kPa
siCTRL
siTLN1+2
Traction (Pa):
0
450
h
22 kPa
Median (siCTRL) = 198.4 nN
Median (siTLN1+2) = 186.7 nN
p (K-S test) = 0.029
Density (×10⁻²)
Total force (nN)
i
MDA-MB-231
Beads (gradient)
Nuclei
siCTRL
siTLN1+2
Soft
(~0.5 kPa)
Stiff
(~22.0 kPa)
y coordinate (×10³)
x coordinate (×10³)
Cell count
j
0.5 kPa
22.0 kPa
siCTRL
siTLN1+2
p < 0.001
p = 0.008
Norm. cell density (a.u.)
Norm. bead fluorescence (a.u.)

positive durotaxis in the 2–18 kPa range[8]. Talin knockdown (Fig. 5b and Supplementary Figs. 13a and 17) resulted in significantly fewer and smaller FAs (Fig. 5c–e and Supplementary Fig. 13b,c) and reduced traction on ~20 kPa substrates, where adhesion reinforcement is expected to counteract clutch dissociation by rapidly accumulating forces (Fig. 5f–h and Supplementary Fig. 14a). EdU incorporation increased from 0.5 to 9.6 kPa and plateaued thereafter, with and without talin silencing (Supplementary Fig. 14b,c). Although control MDA-MB-231s seeded on 0.5–22.0 kPa stiffness gradients migrated towards the stiffest regions available, talin-low MDA-MB-231s phenocopied the negative durotaxis observed in U-251MGs and predominantly clustered in regions of intermediate stiffness (Fig. 5i,j and Supplementary Fig. 13d,e). Thus, the familiar positive durotactic behaviour can be converted to negative durotaxis by manipulating the adhesive and contractile machinery of a cell to change its optimal stiffness.

Outlook

The concept of cells moving towards environments where they can exert more traction is intuitive, but has been previously understood in the context of a denser, stiffer ECM providing cells with more stable anchorage[7]. Our results demonstrate the additional capacity of individual cells to migrate towards softer environments, that is, negative durotaxis, which can be explained by a motor–clutch-based model. Cells that lack robust adhesion reinforcement, such as U-251MG glioma cells or talin-low MDA-MB-231 breast cancer cells, tend to exert maximal traction on substrates with intermediate stiffness, and migrate along gradients to reach this optimum by positive or negative durotaxis (Supplementary Fig. 15). The same mechanism is likely to contribute to the recently described neurite growth towards soft matrix[24]. Together with other mechanosensitive cellular responses, such as increased proliferation or overall motility on mechanically distinct substrates[29,43], durotaxis can contribute to a variety of biological processes, including central nervous system development and cancer metastasis. Especially intriguing would be to test ovarian cancer cells that exhibit decreasing traction force with increasing substrate stiffness[43], suggesting the possibility of negative durotaxis over this stiffness range.

Besides directly reinforcing connections to a stiff matrix, mechanosensitive FA formation may promote positive durotaxis by additional mechanisms. Preferential trafficking of adhesion components towards existing FAs[44], local activation of mechanically gated ion channels[45] or other biochemical signalling pathways initiated at the FAs[35] may contribute to the further polarization of cell–matrix adhesion and consequently of the cellular traction forces. How these factors influence the stiffness optima on different substrates, and in different biological conditions, will be an interesting topic for future research. Taken together, our results point to a single, conserved mechanism for stiffness sensing and durotaxis across a broad range of cell types, with motor–clutch dynamics driving traction generation and choices between positive and negative durotaxis.

Online content

Any methods, additional references, Nature Research reporting summaries, source data, extended data, supplementary information, acknowledgements, peer review information; details of author contributions and competing interests; and statements of data and code availability are available at https://doi.org/10.1038/s41563-022-01294-2.

Received: 7 January 2021; Accepted: 18 May 2022;
Published online: 11 July 2022

References

1. Ladoux, B., Mège, R.-M. & Trepat, X. Front–rear polarization by mechanical cues: from single cells to tissues. *Trends Cell Biol.* **26**, 420–433 (2016).
2. Hamidi, H. & Ivaska, J. Every step of the way: integrins in cancer progression and metastasis. *Nat. Rev. Cancer* **18**, 533–548 (2018).
3. Lo, C. M., Wang, H. B., Dembo, M. & Wang, Y. L. Cell movement is guided by the rigidity of the substrate. *Biophys. J.* **79**, 144–152 (2000).
4. Isenberg, B. C., DiMilla, P. A., Walker, M., Kim, S. & Wong, J. Y. Vascular smooth muscle cell durotaxis depends on substrate stiffness gradient strength. *Biophys. J.* **97**, 1313–1322 (2009).
5. Plotnikov, S. V., Pasapera, A. M., Sabass, B. & Waterman, C. M. Force fluctuations within focal adhesions mediate ECM-rigidity sensing to guide directed cell migration. *Cell* **151**, 1513–1527 (2012).
6. Breckenridge, M. T., Desai, R. A., Yang, M. T., Fu, J. & Chen, C. S. Substrates with engineered step changes in rigidity induce traction force polarity and durotaxis. *Cell. Mol. Bioeng.* **7**, 26–34 (2014).
7. Sunyer, R. et al. Collective cell durotaxis emerges from long-range intercellular force transmission. *Science* **353**, 1157–1161 (2016).
8. DuChez, B. J., Doyle, A. D., Dimitriadis, E. K. & Yamada, K. M. Durotaxis by human cancer cells. *Biophys. J.* **116**, 670–683 (2019).
9. Barriga, E. H., Franze, K., Charras, G. & Mayor, R. Tissue stiffening coordinates morphogenesis by triggering collective cell migration in vivo. *Nature* **554**, 523–527 (2018).
10. Zhu, M. et al. Spatial mapping of tissue properties in vivo reveals a 3D stiffness gradient in the mouse limb bud. *Proc. Natl Acad. Sci. USA* **117**, 4781–4791 (2020).
11. McKenzie, A. J. et al. The mechanical microenvironment regulates ovarian cancer cell morphology, migration, and spheroid disaggregation. *Sci. Rep.* **8**, 7228 (2018).
12. Yeoman, B. et al. Adhesion strength and contractility enable metastatic cells to become adurotactic. *Cell Rep.* **34**, 108816 (2021).
13. Hartman, C. D., Isenberg, B. C., Chua, S. G. & Wong, J. Y. Vascular smooth muscle cell durotaxis depends on extracellular matrix composition. *Proc. Natl Acad. Sci. USA* **113**, 11190–11195 (2016).
14. Lachowski, D. et al. FAK controls the mechanical activation of YAP, a transcriptional regulator required for durotaxis. *FASEB J.* **32**, 1099–1107 (2018).
15. Puleo, J. I. et al. Mechanosensing during directed cell migration requires dynamic actin polymerization at focal adhesions. *J. Cell Biol.* **218**, 4215–4235 (2019).
16. Abercrombie, M. The Croonian Lecture, 1978—the crawling movement of metazoan cells. *Proc. R. Soc. Lond. B* **207**, 129–147 (1980).
17. Mitchison, T. & Kirschner, M. Cytoskeletal dynamics and nerve growth. *Neuron* **1**, 761–772 (1988).
18. Chan, C. E. & Odde, D. J. Traction dynamics of filopodia on compliant substrates. *Science* **322**, 1687–1691 (2008).
19. Elosegui-Artola, A. et al. Mechanical regulation of a molecular clutch defines force transmission and transduction in response to matrix rigidity. *Nat. Cell Biol.* **18**, 540–548 (2016).
20. DiMilla, P. A., Barbee, K. & Lauffenburger, D. A. Mathematical model for the effects of adhesion and mechanics on cell migration speed. *Biophys. J.* **60**, 15–37 (1991).
21. Klank, R. L. et al. Biphasic dependence of glioma survival and cell migration on CD44 expression level. *Cell Rep.* **18**, 23–31 (2017).
22. Rens, E. G. & Merks, R. M. H. Cell shape and durotaxis explained from cell-extracellular matrix forces and focal adhesion dynamics. *iScience* **23**, 101488 (2020).
23. Schmidt, C. E., Dai, J., Lauffenburger, D. A., Sheetz, M. P. & Horwitz, A. F. Integrin-cytoskeletal interactions in neuronal growth cones. *J. Neurosci.* **15**, 3400–3407 (1995).
24. Koser, D. E. et al. Mechanosensing is critical for axon growth in the developing brain. *Nat. Neurosci.* **19**, 1592–1598 (2016).
25. Franze, K. Integrating chemistry and mechanics: the forces driving axon growth. *Annu. Rev. Cell Dev. Biol.* **36**, 61–83 (2020).
26. Bangasser, B. L. & Odde, D. J. Master equation-based analysis of a motor-clutch model for cell traction force. *Cell. Mol. Bioeng.* **6**, 449–459 (2013).
27. Bangasser, B. L., Rosenfeld, S. S. & Odde, D. J. Determinants of maximal force transmission in a motor-clutch model of cell traction in a compliant microenvironment. *Biophys. J.* **105**, 581–592 (2013).
28. Cheng, B. et al. An integrated stochastic model of matrix-stiffness-dependent filopodial dynamics. *Biophys. J.* **111**, 2051–2061 (2016).
29. Bangasser, B. L. et al. Shifting the optimal stiffness for cell migration. *Nat. Commun.* **8**, 15313 (2017).
30. Lerche, M. et al. Integrin binding dynamics modulate ligand-specific mechanosensing in mammary gland fibroblasts. *iScience* **23**, 100907 (2020).
31. Barber-Pérez, N. et al. Mechano-responsiveness of fibrillar adhesions on stiffness-gradient gels. *J. Cell Sci.* **133**, jcs242909 (2020).
32. Miroshnikova, Y. A. et al. Tissue mechanics promote IDH1-dependent HIF1α–tenascin C feedback to regulate glioblastoma aggression. *Nat. Cell Biol.* **18**, 1336–1345 (2016).
33. Kechagia, J. Z., Ivaska, J. & Roca-Cusachs, P. Integrins as biomechanical sensors of the microenvironment. *Nat. Rev. Mol. Cell Biol.* **20**, 457–473 (2019).
34. Atherton, P. et al. Vinculin controls talin engagement with the actomyosin machinery. *Nat. Commun.* **6**, 10038 (2015).

35. Cheng, B. et al. Nanoscale integrin cluster dynamics controls cellular mechanosensing via FAKY397 phosphorylation. *Sci. Adv.* **6**, eaax1909 (2020).
36. Kanchanawong, P. et al. Nanoscale architecture of integrin-based cell adhesions. *Nature* **468**, 580–584 (2010).
37. Mason, D. E. et al. YAP and TAZ limit cytoskeletal and focal adhesion maturation to enable persistent cell motility. *J. Cell Biol.* **218**, 1369–1389 (2019).
38. Hou, J. C. et al. Modeling distributed forces within cell adhesions of varying size on continuous substrates. *Cytoskeleton* **76**, 571–585 (2019).
39. Betz, T., Koch, D., Lu, Y.-B., Franze, K. & Käs, J. A. Growth cones as soft and weak force generators. *Proc. Natl Acad. Sci. USA* **108**, 13420–13425 (2011).
40. Koch, D., Rosoff, W. J., Jiang, J., Geller, H. M. & Urbach, J. S. Strength in the periphery: growth cone biomechanics and substrate rigidity response in peripheral and central nervous system neurons. *Biophys. J.* **102**, 452–460 (2012).
41. Ghibaudo, M. et al. Traction forces and rigidity sensing regulate cell functions. *Soft Matter* **4**, 1836–1843 (2008).
42. Kuipers, A. J. et al. TRPM7 controls mesenchymal features of breast cancer cells by tensional regulation of SOX4. *Biochim. Biophys. Acta Mol. Basis Dis.* **1864**, 2409–2419 (2018).
43. McGrail, D. J., Kieu, Q. M. N. & Dawson, M. R. The malignancy of metastatic ovarian cancer cells is increased on soft matrices through a mechanosensitive Rho–ROCK pathway. *J. Cell Sci.* **127**, 2621–2626 (2014).
44. Fourriere, L. et al. RAB6 and microtubules restrict protein secretion to focal adhesions. *J. Cell Biol.* **218**, 2215–2231 (2019).
45. Kobayashi, T. & Sokabe, M. Sensing substrate rigidity by mechanosensitive ion channels with stress fibers and focal adhesions. *Curr. Opin. Cell Biol.* **22**, 669–676 (2010).

Methods

Cell culture, reagents and transfections. U-251MG human glioblastoma cells were obtained from G. Y. Gillespie (The University of Alabama at Birmingham), authenticated using a short tandem repeat assay (University of Arizona Genetics Core) and cultured in Dulbecco's modified Eagle's medium (DMEM)/F-12 (Gibco, 11320-074) supplemented with 8% foetal bovine serum (Sigma, F7524). MDA-MB-231 human breast adenocarcinoma cells were purchased from American Type Culture Collection and authenticated using a short tandem repeat assay (Leibniz Institute DSMZ—German Collection of Microorganisms and Cell Cultures). U-2 OS human osteosarcoma cells were acquired from DSMZ. Both MDA-MB-231 and U-2 OS were cultured in high-glucose DMEM (Sigma, D5796-500ML) supplemented with 10% foetal bovine serum (Sigma, F7524), 2 mM L-glutamine (Sigma, G7513-100ML) and ×1 non-essential amino acids (Sigma, M7145-100 ML). The cells were tested for mycoplasma contamination and cultured at +37 °C, 5% CO_2 in a humidified incubator. ROCK1/2 inhibitor H-1152 was acquired from Calbiochem (Merck Millipore, 555550) and myosin II inhibitor (−)-blebbistatin was acquired from STEMCELL Technologies (72402).

For the transient downregulation of target proteins, the cells were transfected with the corresponding siRNAs at a 50 nM concentration per oligo. The transfections were conducted using Opti-MEM reduced serum medium (Thermo Fisher Scientific, 31985-047) and Lipofectamine RNAiMAX reagent (Thermo Fisher Scientific, 56532) according to the manufacturer's instructions. The siRNAs used were Hs_TLN1_3 FlexiTube siRNA (Qiagen, SI00086975), Hs_TLN1_2 FlexiTube siRNA (Qiagen, SI00086968), Hs_TLN2_3 FlexiTube siRNA (Qiagen, SI00109277), Dharmacon ON-TARGETplus Human TLN2 (83660) (Horizon Discovery, J-012909-05-0002) and AllStars Negative Control siRNA (Qiagen, 1027281). The silenced cells were grown for 24 (beginning of migration experiments) to 72 h before they were used for experiments.

Antibodies. The following antibodies were used at the indicated dilutions: ms anti-paxillin (BD Biosciences, 612405, 1:200 for immunofluorescence (IF)), rbt anti-paxillin (Santa Cruz Biotechnology, sc-5574, 1:200 for IF), ms anti-vinculin (Sigma, V9131, 1:200 for IF, 1:1,000 for western blotting (WB)), ms anti-talin-1 (Novus, NBP2-50320, 1:1,000 for WB), ms anti-talin-2 (Novus, NBP2-50322, 1:1,000 for WB), ms anti-FAK (BD Biosciences, 610088, 1:1,000 for WB), rbt anti-p-FAK (Y397) (Cell Signaling Technology, 8556, 1:100 for IF, 1:1,000 for WB), rbt anti-MLC2 (Cell Signaling Technology, 3672, 1:1,000 for WB), rbt anti-p-MLC2 (T18/S19) (Cell Signaling Technology, 3674, 1:1,000 for WB), rbt anti-ERK1/2 (Cell Signaling Technology, 9102, 1:1,000 for WB), rbt anti-p-ERK1/2 (T202/Y204) (Cell Signaling Technology, 4370, 1:1,000 for WB), ms anti-YAP (Santa Cruz Biotechnology, sc-101199, 1:200 for IF), rbt anti-vimentin (Cell Signaling Technology, 5741, 1:1,000 for WB), ms anti-GAPDH (HyTest, MAb 6C5, 1:5,000 for WB), rbt anti-fibronectin (Sigma, F3648, 1:500 for IF), ms anti-active β1-integrin (clone 12G10, in-house production, 5 μg ml^{-1} for IF), rat anti-inactive β1-integrin (clone Mab13, in-house production, 10 μg ml^{-1} for cell culture) and normal rat IgG2a kappa isotype control (eBioscience, 14-4321-85, 10 μg ml^{-1} for cell culture).

Additionally, the following secondary antibodies were used for IF and immunoblots at the indicated dilutions: Alexa Fluor 488/568–conjugated secondary antibodies raised against mouse (Invitrogen, A21202 and A10037, 1:400 for IF) and rabbit (Invitrogen, A21206 and A10042, 1:400 for IF), IRDye 800CW donkey anti-mouse IgG (LI-COR Biosciences, 926-32212, 1:5,000 for WB), IRDye 800CW donkey anti-rabbit IgG (LI-COR Biosciences, 926-32213, 1:5,000 for WB) and IRDye 680LT donkey anti-mouse IgG (LI-COR Biosciences, 926-68022, 1:5,000 for WB).

EdU incorporation assay. To measure the rate of EdU incorporation into DNA, the cells were grown on hydrogels for 24 h, after which they were prepared into fluorescence microscopy samples using an EdU proliferation assay kit (Abcam, ab222421) according to the manufacturer's instructions. Briefly, the cells were supplemented with 20 μM EdU for 2 h, fixed and permeabilized, and the EdU was stained with iFluor 647 azide via a copper-catalysed click reaction. The nuclei were counterstained before imaging (see below).

Blocking β1-integrin function with antibodies. U-251MG cells were grown on 0.5 kPa and 60.0 kPa hydrogels for 24 h, after which they were treated with 10 μg ml^{-1} of anti-inactive β1-integrin (that is, function-blocking) clone Mab13 or normal rat isotype control for 2 h (the list of antibodies provides further details). The cells were fixed and processed for IF imaging.

Cell migration on stiffness gradient substrates. For the analysis of cell migration on continuous 0.5–22.0 kPa stiffness gradients, 15,000 (MDA-MB-231)–20,000 (U-251MG) cells were seeded on a fibronectin-functionalized stiffness gradient hydrogel. An even distribution of cells in the beginning of the experiment was confirmed visually (via bright-field microscopy) and by recording the positions of individual nuclei along the gradient using SiR-DNA. The plate was returned to the incubator for 48 h (U-251MG) or 72 h (MDA-MB-231), after which the cells were fixed and the nuclei were revisualized with 4',6-diamidino-2-phenylindole (DAPI). Alternatively, 30,000 U-251MG cells were seeded on a stiffness gradient and left to adhere for one hour. For inhibitor experiments, the culture was then supplemented with 1–5 μM H-1152, 5–25 μM blebbistatin or vehicle (dimethyl sulfoxide (DMSO)). Imaging was started two to three hours after seeding and time-lapse movies were acquired overnight at 15 min intervals. After the experiment was finished, the culture was fixed and prepared for IF imaging (vinculin and phosphorylated MLC2), as described below. Migration tracks from individual cells were analysed for angular displacements and forward migration indices (defined here as Δy/total accumulated distance, where positive values correlate with migration towards the stiffer substrate).

For live-cell imaging of U-251MG migration on photoresponsive stiffness gradient hydrogels, 10,000 cells were seeded per dish and allowed to settle in the incubator for 30 min before imaging. Time-lapse movies were acquired at 20 or 30 min intervals for 45–60 h. The number of cells in the soft and stiff regions of the gel, in the beginning and end of the experiment, was quantified. Additionally, the movies were analysed for cells directly on top of a stiffness gradient. Such cells were tracked over time to investigate their bias for migrating towards either stiffness. Mitotic, dying or crowded cells were excluded from the analysis.

Western blotting. Cells on hydrogels were placed on ice, rinsed twice with ice-cold phosphate-buffered saline (PBS) and scraped into a lysis buffer (50 mM Tris-HCl (pH 7.5), 150 mM NaCl, 1.0% sodium dodecyl sulfate (SDS), 0.5% Triton X-100, 5.0% glycerol, supplemented with protease (Roche, 05056489001) and phosphatase (Roche, 04906837001) inhibitors). The lysates were vortexed, placed on a heat block (+90 °C) for 10 min and sonicated before separation by SDS–polyacrylamide gel electrophoresis (4–20% Mini-PROTEAN TGX gels, Bio-Rad, 456-1096). Next, the proteins were transferred to nitrocellulose membranes and visualized using a 1% Ponceau S staining solution. The membranes were blocked with 5% skimmed milk in tris-buffered saline and 0.1% Tween 20 and incubated with the indicated primary antibodies overnight at +4 °C, followed by fluorophore-conjugated secondary antibodies for 1–2 h at room temperature. All the antibodies were diluted in the StartingBlock blocking buffer (Thermo Fisher Scientific, 37538). Finally, the membranes were scanned using an Odyssey infrared imaging system (LI-COR Biosciences).

Conventional polyacrylamide hydrogels. Glass-bottom dishes (Cellvis, D35-14-1-N) were treated for 20 min at room temperature with 100 μl Bind-Silane solution—a mixture of 3-(trimethoxysilyl)propylmethacrylate (7.15% by volume, Sigma-Aldrich, M6514) and acetic acid (7.15% by volume) in absolute ethanol—to promote gel attachment to the glass surface. After Bind-Silane was aspirated, the glass was washed twice with ethanol and left to dry completely. For homogeneous (constant Young's modulus) hydrogels, predefined ratios of 40% (w/v) acrylamide (Sigma-Aldrich, A4058) and 2% (w/v) *N*,*N*-methyl-bis-acrylamide (Sigma-Aldrich, M1533) were mixed in PBS on ice and carefully vortexed. The final concentrations were adjusted to yield the desired Young's modulus (Supplementary Table 1). Gels that were indicated for traction force microscopy were supplemented with additional 0.2 μm yellow–green fluorescent (505/515) microspheres (~1.5×10^{10} ml^{-1} final concentration, Invitrogen, F8811), which were sonicated for 3 min before use. Polymerization was initiated by the addition of 10% ammonium persulfate (final 0.1% by volume, Bio-Rad) and *N*,*N*,*N*′,*N*′-tetramethylethylenediamine (final 0.2% by volume, Sigma-Aldrich, T-9281) to the solution. Immediately afterwards, 13 μl solution was pipetted onto the glass-bottom dish and a 13 mm circular coverslip was placed on top of the droplet. After polymerization for ~1 h at room temperature, the gel was immersed in PBS for 5 min, the top coverslip was gently removed and the gel was washed twice with PBS to remove any excess acrylamide. Hydrogels with continuous two-dimensional stiffness gradients were fabricated, as described previously[31]. Briefly, 0.5 kPa and 22.0 kPa acrylamide prepolymer solutions were prepared and 0.1 μm fluorescent (505/515) microspheres (~1.2×10^{11} ml^{-1} final concentration, Invitrogen, F8803) were added to the 22 kPa solution. After polymerization was initiated, the two solutions were allowed to diffuse together on a glass-bottom dish, under a glass coverslip, to yield a gradient wherein the microsphere density linearly correlates with the Young's modulus of the substrate.

Before use, the hydrogels were activated by a combination of 0.2 mg ml^{-1} Sulfo-SANPAH (Thermo Fisher Scientific, 22589) and 2 mg ml^{-1} *N*-(3-dimethylaminopropyl)-*N*′-ethylcarbodiimidehydrochloride (Sigma-Aldrich, 03450) in 50 mM 4-(2-hydroxyethyl)piperazine-1-ethanesulfonic acid. A total of 500 μl solution was added on top of the hydrogel and incubated for 30 min at room temperature, protected from light and subjected to gentle agitation. The gel and solution were then ultraviolet (UV) irradiated for 10 min (28–32 mW cm^{-2}) to activate the Sulfo-SANPAH, and the plate was washed with PBS three times to remove any residual compounds. Finally, each hydrogel was functionalized by incubation in 10 μg ml^{-1} fibronectin solution overnight at +4 °C.

Cells that were collected for protein lysates were cultured on commercial hydrogel-coated six-well plates (Matrigen, SW6-EC-0.5/SW6-EC-8/SW6-EC-50). These gels were similarly coated with 10 μg ml^{-1} of fibronectin before use.

Synthesis of o-NBbA. *2-Nitro-4-ethyl aniline (S2).* Here p-ethyl aniline (5 g, 41.3 mmol) was added dropwise to a cold solution of concentrated H_2SO_4 (30 ml) and stirred for 5 min. In a separate flask, 5.3 ml of 70% HNO_3 (82.6 mmol)

was mixed with an equal volume of H_2SO_4, and added dropwise to the reaction vessel, followed by 15 min stirring at 0 °C. Thin-layer chromatography (TLC) analysis (Hex:EtOAc, 2:1, v/v) indicated the complete conversion to the product. The reaction was quenched by pouring the mixture into 200 ml ice water. The resulting precipitate was filtered and washed with H_2O to yield compound **S2** (6.2 g, 90%).

^{1}H NMR (500 MHz, $CDCl_3$) δ ppm 1.099 (t, J=7.5 Hz, 3H), 2.612 (q, J=7.0 Hz, 2H), 5.558 (s, 2H), 6.804 (dd, J=8.0, 2.5 Hz, 1H), 7.041 (d, J=2.5 Hz, 1H), 7.095 (d, J=8.5 Hz, 1H)

^{13}C NMR (100 MHz, DMSO-d6) 149.3411, 147.8646, 131.6051, 124.0586, 118.8417, 107.9194, 24.4890, 15.3093

HRMS (*m*/*z*): $[M]^+$ calcd for $[C_8H_{10}N_2O_2]^+$ 166.0737, found 166.0737.

4-Ethyl-3-nitrophenol (S3). Compound **S2** (6.2 g, 37.3 mmol) was suspended in a mixture of H_2SO_4 and H_2O (1:3, v/v, 25–50 ml) by sonication (if sonication did not yield a homogenous suspension, a few millilitres of tetrahydrofuran (THF) was used to dissolve solid **S2**, which was then added to the mixture of aqueous H_2SO_4). $NaNO_2$ (3.86 g, 56.0 mmol) dissolved in H_2O (2.5 ml) was slowly added to the reaction flask and stirred at room temperature for 1.5 h. In a separate flask, H_2SO_4:H_2O (4:3, v/v, 75 ml) was added and heated to reflux. To the refluxing mixture, **S2** solution was added dropwise and stirred for 30 min. The mixture was quenched with ice water and extracted with EtOAc (3×75 ml). After drying the organic layer with Mg_2SO_4, the solvent was removed in vacuo and the crude product was purified by silica-gel flash column chromatography (Hex:EtOAc, 2:1) to give **S3** (3.11 g, 50%) as a yellow oil.

^{1}H NMR (500 MHz, $CDCl_3$) δ ppm 1.249 (t, J=7.5 Hz, 3H), 2.842 (q, J=8.5 Hz, 2H), 7.030 (dd, J=8.5, 2.5 Hz, 1H), 7.230 (d, J=8.5 Hz, 1H), 7.383 (d, J=2.5 Hz, 1H)

^{13}C NMR (100 MHz, $CDCl_3$) 154.2470, 149.5150, 132.3914, 131.3014, 120.7326, 111.4436, 25.6617, 15.1987

HRMS (*m*/*z*): $[M-H]^-$ calcd for $[C_8H_8NO_3]^-$ 166.0510, found 166.0524.

tert-Butyl 2-(4-ethyl-3-nitrophenoxy)acetate (S4). Compound **S3** (3.11 g, 18.6 mmol) and tert-butyl 2-bromoacetate (4.35 g, 22.3 mmol) were dissolved in DMF (25 ml). Solid K_2CO_3 (5.14 g, 37.2 mmol) was added to the reaction flask and left to stir at +70 °C for 1.5 h until TLC analysis (2:1 Hex:EtOAc, v/v) indicated the complete conversion to the product. The solvent was removed in vacuo and redissolved in 100 ml EtOAc. The organic layer was washed with saturated NH_4Cl (50 ml) and brine and then dried over Na_2SO_4. Solvent removal in vacuo afforded **S4** (4.97 g, 95%) as a yellow oil.

^{1}H NMR (500 MHz, $CDCl_3$) δ ppm 1.253 (t, J=7.5 Hz, 3H), 1.5 (s, 9H), 2.857 (q, J=7.5 Hz, 2H), 4.554 (s, 2H), 7.116 (dd, J=8.5, 2.5 Hz, 1H), 7.277 (d, J=8.5 Hz, 1H), 7.391 (d, J=3 Hz, 1H)

^{13}C NMR (100 MHz, $CDCl_3$) 167.3932, 156.3652, 149.4567, 132.3149, 132.2128, 120.6270, 110.0036, 83.0951, 66.0518, 28.1809, 25.7638, 15.1222

HRMS (*m*/*z*): $[M+Na]^+$ calcd for $[C_{14}H_{19}NO_5Na]^+$ 304.1155, found 304.1160.

tert-Butyl 2-(4-(1-bromoethyl)-3-nitrophenoxy)acetate (S5). Compound **S4** (4.97 g, 17.7 mmol), *N*-bromosuccinimide (3.8 g, 19.5 mmol) and benzoylperoxide (0.2 g, 1 mmol) were dissolved in CCl_4 (100 ml) and refluxed for 4 h. The reaction mixture was cooled to room temperature and washed with 0.1% $NaHCO_3$ (aq) and brine and then dried over Na_2SO_4. The solvent was removed in vacuo and the crude product was purified by silica-gel flash column chromatography (3:1 Hex:EtOAc, v/v) to afford **S5** (5.7 g, 90%) as a yellow oil.

^{1}H NMR (500 MHz, $CDCl_3$) δ ppm 1.498 (s, 9H), 2.054 (d, J=7 Hz, 3H), 4.571 (s, 2H), 5.787 (q, J=7 Hz, 1H), 7.184 (dd, J=8.5, 3 Hz, 1H), 7.299 (d, J=2.5 Hz, 1H), 7.784 (d, J=9 Hz, 1H)

^{13}C NMR (100 MHz, $CDCl_3$) 167.0028, 157.7588, 148.0010, 131.1486, 130.8123, 120.7031, 109.7326, 83.3722, 66.0153, 42.0634, 28.1845, 27.3715

HRMS (*m*/*z*): $[M-Br]^+$ calcd for $[C_{14}H_{18}NO_5]^+$ 280.1179, found 280.1163.

2-(4-(1-Bromoethyl)-3-nitrophenoxy)ethan-1-ol (S6). Compound **S5** (5.7 g, 15.9 mmol) was dissolved in 100 ml THF and cooled down to −78 °C. Diisobutylaluminium hydride (39.8 mmol) was added to the reaction flask and stirred at −78 °C for 20 min and then left to stir for an additional 2 h at 0 °C. TLC analysis (3:1 Hex:EtOAc, v/v) essentially indicated the complete conversion to the product. The reaction was quenched by slowly adding 30 ml H_2O to the mixture, followed by the addition of 5% HCl (aq) solution until the aqueous solution became acidic (pH ~4, as judged by pH paper). After vigorously mixing the biphasic mixture in a separatory funnel, the separated organic layer was washed with brine and then dried over Na_2SO_4. The solvent was removed in vacuo and the crude product was purified by silica-gel flash column chromatography to yield **S6** (3.23 g, 60%) as a yellow oil.

^{1}H NMR (500 MHz, $CDCl_3$) δ ppm 2.056 (d, J=5 Hz, 3H), 4.006 (dd, J=4.5, 4.5 Hz, 2H), 4.142 (dd, J=4, 4 Hz, 2H), 5.785 (q, J=7 Hz, 1H), 7.201 (dd, J=8.5, 2.5 Hz, 1H), 7.356 (d, J=2.5 Hz, 1H), 7.783 (d, J=8.5 Hz, 1H)

^{13}C NMR (100 MHz, $CDCl_3$) 158.5634, 148.1515, 131.0462, 130.2806, 120.5139, 109.6535, 70.1749, 61.2504, 42.1290, 27.3423

HRMS (*m*/*z*): $[M-Br]^+$ calcd for $[C_{14}H_{18}NO_5]^+$ 210.0761, found 210.0761.

1-(4-(2-Hydroxyethoxy)-2-nitrophenyl)ethan-1-ol (S7). **S6** (3.23 g, 11.1 mmol) was dissolved in 250 ml H_2O and refluxed for 1 h. TLC analysis (1:1 Hex:EtOAc, v/v) essentially indicated the complete conversion to the product. The product was extracted with EtOAc (3×50 ml). The organic layer was washed with brine and then dried over Na_2SO_4. The solvent was evaporated in vacuo and **S7** (2.0 g, 80%) was used for the next step without further purification.

^{1}H NMR (500 MHz, $CDCl_3$) δ ppm 1.540 (d, J=6.4 Hz, 3H), 3.997 (dd, J=4.6, 4.6 Hz, 2H), 4.120 (dd, J=7.1, 7.1 Hz, 2H), 5.341 (q, J=6.2 Hz, 1H), 7.201 (dd, J=8.8, 2.8 Hz, 1H), 7.410 (d, J=2.7 Hz, 1H), 7.734 (d, J=8.8 Hz, 1H)

1-(4-(2-(Acryloyloxy)ethoxy)-2-nitrophenyl)ethyl acrylate (o-NBbA, S8). To a solution of **S7** (2.0 g, 8.88 mmol) and acryloyl chloride (26.6 mmol) in CH_2Cl_2 (75 ml), triethylamine (3.5 eq) was added and the mixture was stirred at room temperature for 24 h. The mixture was washed with H_2O and brine and then dried over Na_2SO_4. The solvent was evaporated in vacuo and the crude material was purified by silica-gel flash column chromatography (2.5:1 Hex:EtOAc, v/v) to yield **S8** (1.79 g, 60%) as a yellow oil.

^{1}H NMR (500 MHz, $CDCl_3$) δ ppm 1.653 (d, J=6.5 Hz, 3H), 4.253–4.272 (m, 2H), 4.517–4.536 (m, 2H), 5.849 (dd, J=16.5, 1.5 Hz, 1H), 5.87 (dd, J=16.5, 1.5 Hz, 1H), 6.135 (dd, J=33, 10.5 Hz, 1H), 6.135 (dd, J=10.5, 1.5 Hz, 1H), 6.333 (dd, J=6.5, 6.5 Hz, 1H), 6.425 (dd, J=38.5, 1.5 Hz, 1H), 6.425 (dd, J=4, 1 Hz, 1H), 7.181 (dd, J=8.5, 2.5 Hz, 1H), 7.471 (d, J=2.5 Hz, 1H), 7.547 (d, J=8.5 Hz, 1H)

^{13}C NMR (100 MHz, DMSO-d6) 165.3601, 164.6091, 157.8246, 148.5720, 132.2687, 132.0463, 128.7689, 128.2840, 127.9741, 127.9522, 120.6063, 109.4215, 67.2670, 66.6545, 62.5167, 21.2189

HRMS (*m*/*z*): $[M+Na]^+$ calcd for $[C_{16}H_{17}NO_7Na]^+$ 358.0897, found 358.0888.

Fabrication of photoresponsive polyacrylamide hydrogels. Photoresponsive polyacrylamide gel substrates were prepared based on a previously reported method[46]. Briefly, high Grid-500 glass-bottom dishes (Fischer, 50-305-810) were activated for gel attachment by sequential treatment with 0.1 M NaOH, 97% (3-aminoproyl)trimethoxysilane (Sigma-Aldrich, 281778) and 0.5% glutaraldehyde (Polysciences, 01909). A prepolymer mixture of 40% (w/v) acrylamide solution (25% by volume, Fisher, BP1402), 2% (w/v) bis-acrylamide solution (2.5% by volume, Fisher, BP1404), 50 mM o-nitrobenzyl bis-acrylate (in DMSO, 3.25% by volume), 1 M 4-(2-hydroxyethyl)piperazine-1-ethanesulfonic acid (pH 7, 1% by volume, Sigma-Aldrich, H6147) solution, 71.7 mM acrylic acid *N*-hydroxysuccinimide ester (in DMSO, 4% by volume, Sigma-Aldrich, A8060) and H_2O (63.25% by volume) was prepared. After degassing for 30 min, polymerization was initiated by adding 10% (w/v) ammonium persulfate (0.6% by volume, Bio-Rad, 161-0700) solution and *N*,*N*,*N*′,*N*′-tetramethylethylenediamine (0.4% by volume, Fisher, BP150). Immediately after initiation, 200 µl gel solution was pipetted onto the activated glass culture dish and covered with a fibronectin-patterned glass coverslip face down (fabricated as described below). After 30 min of polymerization, PBS was added on the dish and the coverslip was removed. Finally, the gel was washed with PBS.

Preparation of one-dimensional fibronectin micropatterns. One-dimensional lines of fibronectin were created on the photoresponsive hydrogels following a microcontact printing method widely applied in the field of surface protein fabrication[47]. Briefly, polydimethylsiloxane stamps fabricated by photolithography and containing topographical patterns (21 µm width, 40 µm spacing) were obtained from the M. Piel laboratory (Institut Curie) and used as received[48]. The patterned side of the stamp was inked with 100 µg ml^{-1} fibronectin (Sigma-Aldrich, F1141) for 1 h. After drying the stamp using a stream of air, the fibronectin-coated stamp was stamped onto a 12 mm no. 1.5 circular coverslip (Fisher, 12-545-80), rinsed with ethanol and treated with plasma (Harrick Plasma) for 60 s, and a 20 g weight was placed on top of the stamp. The fibronectin pattern was finally transferred to the gel surface by placing the coverslip face down on the prepolymer solution as described above, immediately on the initiation of polymerization.

Fabrication of steep stiffness gradients by controlled UV exposure. Stiffness patterns were fabricated on photoresponsive hydrogels using a Nikon ECLIPSE Ti-E epifluorescence microscope and Plan Fluor ×10/0.30 numerical aperture objective (Nikon), controlled by NIS-Elements AR 4.60 software (Nikon). The fibronectin-patterned photoresponsive gel was placed on the stage and using phase-contrast imaging, two regions were selected such that they were '*A*' mm (A > 2) apart. A hypothetical line connecting the two regions ran perpendicularly across the fibronectin patterns (Supplementary Fig. 5a). The field diaphragm lever was then adjusted so that the diameter of the illuminated area on the substrate was 500 µm. Fluorescence imaging using a 395/25 nm light-emitting diode (315 mW) and DAPI filter set with light-emitting diode fluorescence illumination from a Spectra X light engine (Lumencor) was initiated, and a time-lapse movie of the two regions was captured at 0 s intervals for '15×*A*' min, leaving the active shutter open during stage movement. This led to a 500 µm×'*A*' mm region being photoirradiated to the extent that all the photolabile crosslinkers in the exposed region were cleaved. The process was repeated in the regions parallel to and 500 µm apart from the first irradiated area, resulting in a gel that had alternating, 500-µm-wide stiff (~15 kPa) and soft (~8 kPa) regions.

Stiffness characterization by bead indentation. The irradiation time-dependent change in the Young's modulus of the photoresponsive polyacrylamide gel was

measured using a bead indentation method[18] based on Hertzian indentation theory. A thick (>1 mm) hydrogel was created by pipetting 300 µl prepolymer solution onto an activated glass culture dish and covering it with a 25 mm no. 1.5 circular coverslip (Fisher, 12-545-102). After polymerization, the coverslip was removed in PBS and the gel was washed with additional PBS. A silica bead (Polysciences, 1 mm diameter) was placed on the gel after 200 nm crimson fluorospheres were first gravity settled on the gel surface to function as markers for measuring the bead contact area with epifluorescence microscopy. At each irradiation time point, the bead indentation depth (δ) was calculated from the bead radius (R) and contact radius (r) according to equation (1):

$$\delta = R - \sqrt{R^2 - r^2} \quad (1)$$

From this indentation depth, Young's modulus (E) was calculated using the Poisson ratio of the hydrogel (ν) and buoyancy-corrected bead force (f) according to the Hertz solution:

$$E = \frac{3\left(1-\nu^2\right)f}{4R^{1/2}\delta^{3/2}} \quad (2)$$

For polyacrylamide gels, $\nu = 0.3$–0.5 (here $\nu = 0.3$ was used). The glass bead density was measured to be ~2,600 kg m^{-3}.

Immunofluorescence staining. Samples were fixed for 10 min with warm 4% paraformaldehyde, followed by permeabilization and blocking for 20 min with 0.3% Triton X-100 in 10% horse serum (Gibco, 16050-122). Primary antibodies were diluted in 10% horse serum and the samples were incubated with the antibody overnight at +4 °C. Secondary antibodies were diluted in PBS and the samples were incubated with the antibody for 1–2 h at room temperature. Where indicated, the nuclei were counterstained using 5 µg ml^{-1} DAPI or 500 nM SiR-DNA (Spirochrome, SC007; for live cells) and filamentous actin using 200 nM SiR-actin (Spirochrome, SC001).

Fluorescence and bright-field microscopy. Most fluorescent specimens were imaged using a Marianas spinning disk confocal microscope with a Yokogawa CSU-W1 scanning unit, controlled by SlideBook 6 software (Intelligent Imaging Innovations). The objectives used were a ×20/0.8 numerical aperture Plan-APOCHROMAT (ZEISS) and ×40/1.1 W LD C-APOCHROMAT (ZEISS), and the images were acquired using an Orca Flash4.0 sCMOS camera (Hamamatsu Photonics). The two-dimensional stiffness gradient hydrogels with cells were imaged using a Nikon ECLIPSE Ti2-E wide-field microscope, controlled by NIS-Elements AR 5.11 software (Nikon). The objective used was a ×10/0.3 CFI Plan Fluor objective (Nikon), and the images were acquired using an Orca Flash4.0 sCMOS camera (Hamamatsu Photonics) and 2×2 binning. For live-cell tracking on the same substrates, the samples were maintained in a stage-top humidified incubator at +37 °C/5% CO_2.

Live phase-contrast imaging of U-251MG cells on photoresponsive hydrogels was done using a Nikon ECLIPSE Ti-E microscope, controlled by NIS-Elements AR 4.60 software (Nikon). The objective used was a Plan Fluor ×10/0.30 numerical aperture objective (Nikon), and the images were acquired using an Andor Zyla 5.5 sCMOS camera (Andor Technology). The samples were maintained in a Bold Line stage-top humidified incubator (Okolab) at +37 °C/5% CO_2.

Traction force microscopy. To measure the tractions exerted by MDA-MB-231 cells on their substrate, polyacrylamide hydrogels of varying stiffnesses (fibronectin-functionalized and supplemented with fluorescent microbeads) were manufactured on glass-bottom dishes, as described above. The cells were seeded on the gels (5,000 cells per plate) approximately 24 h after transfection with the indicated siRNAs, and grown for another 48 h before the experiment was conducted. For imaging the cells and beads, a Marianas spinning disk confocal microscope with a stage-top incubator unit (+37 °C/5% CO_2) was used. Bright-field images of single cells and fluorescence Z stacks of the beads embedded in the hydrogel were captured before and after cell detachment by the addition of 2% SDS.

The resulting data were analysed using a previously described implementation of Fourier-transform traction cytometry[49]. First, the displacement fields were calculated using high-resolution subsampling and assuming no outward deformation of the substrate. Optimal L2 regularization was performed on the sets of images acquired from soft and stiff gels to determine the final regularization parameter $\lambda = 5\times10^{-6}$, which was then used for calculating all the subsequent traction fields. The background, or noise, of the measurements was estimated by analysing five empty (that is, no cells) fields of view per substrate stiffness.

Finite element analysis. To estimate the effective spring constant around the interface of a stepwise stiffness gradient, a finite element model using COMSOL Multiphysics v.5.3 multibody dynamics module was utilized. Two three-dimensional blocks (120×60×20 µm) were created and interfaced at $x = 0$. Linear elastic material properties were prescribed to both blocks with Poisson's ratio of 0.4, density of 1,000 kg m^{-3} and Young's modulus of 1 and 10 kPa. A lateral 0.5 nN force was applied on a circular (1 µm radius) surface contact (Supplementary Fig. 7a). Fixed boundary conditions were applied to all the surfaces, except the top surface. The displacement field due to applied loads was computed on a model created using built-in automatic meshing routines (extra-fine mechanics-based mesh). These data were used to calculate the effective spring constant at the contact zone (k_{eff} = applied force/average displacement under the circular contact area). The location of the circular contact and direction of the force were varied, and effective spring constants were accordingly calculated (Supplementary Fig. 7b).

Computational modelling of single-cell migration and GC steering on stiffness gradients. A previously described[38] C++ version of the stochastic CMS was modified to account for spatial variations in substrate stiffness and compiled using the GNU Compiler Collection v.4.8. The detailed algorithms and equations governing the base CMS have been comprehensively described elsewhere[29]. Briefly, the CMS uses Gillespie's stochastic simulation algorithm[50] to simulate an entire cell by connecting several motor–clutch modules to a central cell body and then balancing forces at the centre (Fig. 3a). Here the cells were simulated for 60 min to allow them to reach a dynamic steady state, after which each cell was randomly displaced to a 180 µm×180 µm region on a substrate with repeating soft and stiff areas and connecting stiffness gradients (Fig. 3b). Cell positions and traction forces were recorded every second and used to calculate RMC and mean traction force per module. A custom MATLAB (v.R2018b) code was used to quantify the module forces on the soft and stiff substrates, and to track the displacement of individual cells, from gradients or soft regions, over time. All the CMS simulations were conducted at the Minnesota Supercomputing Institute. Supplementary Note 2 and Supplementary Table 2 provide additional details on the cellular-level model and its implementation.

The CMS was further modified to investigate filopodial and GC dynamics on substrate stiffness gradients. The filopodia were represented by individual CMS modules that were arranged around an initially semicircular GC. Each filopodia was allocated a set number of molecular clutches—the corresponding substrate clutches were randomly distributed and their spring constants linearly varied with position along the gradient. Supplementary Note 3 and Supplementary Table 3 present details of the GC model and corresponding simulations.

Image analysis. Images were analysed using ImageJ v.1.52p (National Institutes of Health) and CellProfiler v.2.2.0 (Broad Institute) software. For the analysis of YAP nuclear localization, a custom CellProfiler pipeline was used to segment the cells into nuclei (corresponding to the nuclear counterstain) and cytoplasm (a region of maximum 4 µm around the nucleus, excluding parts outside the cell). The mean grey value in the nucleus was divided by the corresponding value in the cytoplasm. For the analysis of vinculin-positive adhesions in MDA-MB-231s, a semiautomatic ImageJ script was used: an individual confocal plane from the basal side of the cell was subjected to background removal (rolling ball) and thresholding to exclude the cytoplasmic signal and peripheral ruffles. The number and sizes of the remaining adhesions were recorded.

Statistics and reproducibility. Statistical analyses and plotting were performed using GraphPad Prism v.6.05 (GraphPad) and R v.3.5.1 (R Core Team) running on RStudio v.1.3.1073. Confidence intervals for the means were calculated using bias-corrected and accelerated bootstrap intervals from 10,000 resamples. Confidence intervals for binomial data were calculated using the Wilson score interval. Whenever data were deemed to follow a non-normal distribution (according to the Shapiro–Wilk normality test), analyses were conducted using non-parametric methods. The names and/or numbers of individual statistical tests, samples and data points are indicated in the figure legends. Unless otherwise noted, all the results are representative of three independent experiments and two-sided p values have been reported.

Reporting summary. Further information on research design is available in the Nature Research Reporting Summary linked to this article.

Data availability

The data supporting the findings of this study are available within the Article and its Supplementary Information. Other raw data generated during this study are available from the corresponding authors on request. Source data are provided with this paper.

Code availability

All code and scripts used in this study are available online (https://oddelab.umn.edu/ and via GitHub at https://github.com/cbcbcbcb123/Growth-Cone-Dynamics) and on request from the corresponding authors.

References

46. Wang, Y. L. & Pelham, R. J. Preparation of a flexible, porous polyacrylamide substrate for mechanical studies of cultured cells. *Meth. Enzymol.* **298**, 489–496 (1998).
47. Polio, S. R. & Smith, M. L. Patterned hydrogels for simplified measurement of cell traction forces. *Methods Cell. Biol.* **121**, 17–31 (2014).

48. Théry, M. & Piel, M. Adhesive micropatterns for cells: a microcontact printing protocol. *Cold Spring Harb. Protoc.* https://doi.org/10.1101/pdb.prot5255 (2009).
49. Han, S. J., Oak, Y., Groisman, A. & Danuser, G. Traction microscopy to identify force modulation in sub-resolution adhesions. *Nat. Methods* **12**, 653–656 (2015).
50. Gillespie, D. T. Exact stochastic simulation of coupled chemical reactions. *J. Phys. Chem.* **81**, 2340–2361 (1977).

Acknowledgements

We thank L. S. Prahl, J. Tian and G. Huang for helpful discussions on computational modelling and members of the Ivaska Lab for their insightful comments and discussion. Simulations were run in part on the high-performance computing resources at the Minnesota Supercomputing Institute. Turku Bioscience Centre Cell Imaging and Cytometry Core and Biocenter Finland are acknowledged for their services, instrumentation and expertise. We are supported by the University of Turku Doctoral Programme in Molecular Life Sciences (A.I.), the Company of Biologists Travelling Fellowship (A.I.), the Finnish Cultural Foundation (A.I.), the Academy of Finland (AoF CoE 346131 and 325464 (J.I.)), ERC CoG (grant 615258 (J.I.)), Sigrid Juselius Foundation (J.I.), the Finnish Cancer Organization (J.I.), the National Natural Science Foundation of China (11972280 (F.X.); 11772253 (M.L.); 12022206 (M.L.); 11532009 (T.J.L.); 12002262 (B.C.)), Natural Science Basic Research Plan in Shaanxi Province of China (2022KWZ-17 (M.L.)), the Shaanxi Province Youth Talent Support Program (M.L.), the Young Talent Support Plan of Xi'an Jiaotong University (M.L.), the National Institutes of Health (R01 AR077793 (G.M.G.); R01 CA172986 (D.J.O.); U54 CA210190 (D.J.O.); P01 CA254849 (D.J.O.); R35GM141853 (M.D.D.)) and the NSF Science and Technology Center for Engineering Mechanobiology (CMMI 1548571 (G.M.G.)).

Author contributions

A.I., K.-Y.P., J.H., B.C., B.F., J.K., M.L., M.D.D., J.I., D.J.O.: conceptualization. A.I., K.-Y.P., J.H., B.C., M.M.: formal analysis. T.J.L., G.M.G., F.X., M.L., M.D.D., J.I., D.J.O.: funding acquisition. A.I., K.-Y.P., J.H., B.C., M.M., G.A.S., B.F., J.K., M.M.M., F.X.: investigation. A.I., K.-Y.P., J.H., B.F., J.K., M.M.M., T.J.L., G.M.G., F.X., M.L.: methodology. T.J.L., F.X., M.L., M.D.D., J.I., D.J.O.: project administration. T.J.L., G.M.G., F.X., M.L., M.D.D., J.I., D.J.O.: resources. J.H., A.I., B.C., T.J.L., G.M.G., F.X., D.J.O: simulation and modelling. A.I., J.H., B.C., F.X.: software. T.J.L., G.M.G., F.X., M.L., M.D.D., J.I., D.J.O.: supervision. A.I., K.-Y.P., J.H., B.C., M.M., G.M.G., M.L.: validation. A.I., K.-Y.P., J.H., B.C., G.A.S., T.J.L., G.M.G., F.X., M.L.: visualization. A.I., K.-Y.P., J.H., B.C., G.M.G., M.L., M.D.D., J.I., D.J.O.: writing (original draft). All authors: writing (review and editing).

Competing interests

The authors declare no competing interests.

Additional information

Supplementary information The online version contains supplementary material available at https://doi.org/10.1038/s41563-022-01294-2.

Correspondence and requests for materials should be addressed to Min Lin, Mark D. Distefano, Johanna Ivaska or David J. Odde.

Peer review information *Nature Materials* thanks Kenneth Yamada and the other, anonymous, reviewer(s) for their contribution to the peer review of this work.

nature research

Corresponding author(s): Min Lin, Mark D. Distefano, Johanna Ivaska, and David J. Odde

Last updated by author(s): Apr 4, 2022

Reporting Summary

Nature Research wishes to improve the reproducibility of the work that we publish. This form provides structure for consistency and transparency in reporting. For further information on Nature Research policies, see our Editorial Policies and the Editorial Policy Checklist.

Statistics

For all statistical analyses, confirm that the following items are present in the figure legend, table legend, main text, or Methods section.

n/a	Confirmed	
☐	☒	The exact sample size (*n*) for each experimental group/condition, given as a discrete number and unit of measurement
☐	☒	A statement on whether measurements were taken from distinct samples or whether the same sample was measured repeatedly
☐	☒	The statistical test(s) used AND whether they are one- or two-sided *Only common tests should be described solely by name; describe more complex techniques in the Methods section.*
☒	☐	A description of all covariates tested
☐	☒	A description of any assumptions or corrections, such as tests of normality and adjustment for multiple comparisons
☐	☒	A full description of the statistical parameters including central tendency (e.g. means) or other basic estimates (e.g. regression coefficient) AND variation (e.g. standard deviation) or associated estimates of uncertainty (e.g. confidence intervals)
☐	☒	For null hypothesis testing, the test statistic (e.g. *F*, *t*, *r*) with confidence intervals, effect sizes, degrees of freedom and *P* value noted *Give P values as exact values whenever suitable.*
☒	☐	For Bayesian analysis, information on the choice of priors and Markov chain Monte Carlo settings
☒	☐	For hierarchical and complex designs, identification of the appropriate level for tests and full reporting of outcomes
☒	☐	Estimates of effect sizes (e.g. Cohen's *d*, Pearson's *r*), indicating how they were calculated

Our web collection on statistics for biologists contains articles on many of the points above.

Software and code

Policy information about availability of computer code

Data collection	NIS-Elements AR 4.60, 5.11 SlideBook 6.0.18 COMSOL Multiphysics 5.3 GCC 4.8 MATLAB R2014b All custom code and scripts are available online (oddelab.umn.edu and GitHub, https://github.com/cbcbcbcb123/Growth-Cone-Dynamics) or on request from the corresponding authors.
Data analysis	ImageJ/FIJI 1.52p MATLAB R2014b, R2018b CellProfiler 2.2.0 GraphPad Prism 6.05 RStudio 1.3.1073 running R 3.5.1 All custom code and scripts are available online (oddelab.umn.edu and GitHub, https://github.com/cbcbcbcb123/Growth-Cone-Dynamics) or on request from the corresponding authors.

For manuscripts utilizing custom algorithms or software that are central to the research but not yet described in published literature, software must be made available to editors and reviewers. We strongly encourage code deposition in a community repository (e.g. GitHub). See the Nature Research guidelines for submitting code & software for further information.

Data

Policy information about availability of data

All manuscripts must include a data availability statement. This statement should provide the following information, where applicable:

- Accession codes, unique identifiers, or web links for publicly available datasets
- A list of figures that have associated raw data
- A description of any restrictions on data availability

The data supporting the findings of this study are available within the article. Numerical and visual Source Data and Supplementary Data are provided with the paper. Other raw data generated during this study are available from the corresponding authors on request.

Field-specific reporting

Please select the one below that is the best fit for your research. If you are not sure, read the appropriate sections before making your selection.

☒ Life sciences ☐ Behavioural & social sciences ☐ Ecological, evolutionary & environmental sciences

For a reference copy of the document with all sections, see nature.com/documents/nr-reporting-summary-flat.pdf

Life sciences study design

All studies must disclose on these points even when the disclosure is negative.

Sample size	No statistical methods were used to pre-determine sample sizes, which were chosen based on our previous experience on stochastic computational modeling (e.g. Nat Commun. 2017 May 22;8:15313, Sci Adv. 2020 Mar 4;6(10):eaax1909) and in vitro work on cell adhesion and mechanobiology (e.g. Nat Commun. 2017 May 22;8:15313, J Cell Biol. 2017 Apr 3;216(4):1107-1121). For all statistical analyses, three biological replicates was chosen as a self-imposed minimum. The exact replication numbers, sample sizes and statistical methods are described in detail in the text.
Data exclusions	No data were excluded from the analyses.
Replication	All experiments were repeated successfully 2+ times to ensure reproducibility. Key results were reproduced 3+ times, using different batches of reagents and/or consumables (e.g. hydrogel substrates).
Randomization	For experiments conducted using cell lines (same clonal origin), there is no need to account for additional covariates and thus no randomization was used when allocating cells to treatment groups. For immunofluorescence analyses, several fields of view (or cells) were chosen at random and imaged at different locations within each sample.
Blinding	Researchers were unblinded for data analysis. The study did not employ visual stratification of samples to support its conclusions (e.g. evaluation of immunohistochemical stains), and quantitative image and data analyses were automated to minimize the risk of human bias.

Reporting for specific materials, systems and methods

We require information from authors about some types of materials, experimental systems and methods used in many studies. Here, indicate whether each material, system or method listed is relevant to your study. If you are not sure if a list item applies to your research, read the appropriate section before selecting a response.

Materials & experimental systems

n/a	Involved in the study
☐	☒ Antibodies
☐	☒ Eukaryotic cell lines
☒	☐ Palaeontology and archaeology
☒	☐ Animals and other organisms
☒	☐ Human research participants
☒	☐ Clinical data
☒	☐ Dual use research of concern

Methods

n/a	Involved in the study
☒	☐ ChIP-seq
☒	☐ Flow cytometry
☒	☐ MRI-based neuroimaging

Antibodies

Antibodies used	Primary antibodies: anti-paxillin (BD Biosciences, 612405, mouse monoclonal [349], 1:200 for immunofluorescence (IF)), anti-paxillin (Santa Cruz Biotechnology, sc-5574, rabbit polyclonal, 1:200 for IF), anti-vinculin (Sigma, V9131, mouse monoclonal [hVIN-1], 1:200 for IF, 1:1000 for western blotting (WB)), anti-talin-1 (Novus Biologicals, NBP2-50320, mouse monoclonal [97H6], 1:1000 for WB), anti-talin-2 (Novus Biologicals, NBP2-50322, mouse monoclonal [68E7], 1:1000 for WB), anti-FAK (BD Biosciences, 610088, mouse monoclonal [77/FAK], 1:1000 for WB), anti-p-FAK (Y397) (Cell Signaling Technology, 8556, rabbit monoclonal [D20B1], 1:100 for IF,

1:1000 for WB), anti-MLC2 (Cell Signaling Technology, 3672, rabbit polyclonal, 1:1000 for WB), anti-p-MLC2 (T18/S19) (Cell Signaling Technology, 3674, rabbit polyclonal, 1:1000 for WB), anti-ERK1/2 (Cell Signaling Technology, 9102, rabbit polyclonal, 1:1000 for WB), anti-p-ERK1/2 (T202/Y204) (Cell Signaling Technology, 4370, rabbit monoclonal [D13.14.4E], 1:1000 for WB), anti-YAP (Santa Cruz Biotechnology, sc-101199, mouse monoclonal [63.7], 1:200 for IF), anti-vimentin (Cell Signaling Technology, 5741, rabbit monoclonal [D21H3], 1:1000 for WB), anti-GAPDH (HyTest, MAb 6C5, mouse monoclonal [6C5], 1:5000 for WB), anti-fibronectin (Sigma, F3648, rabbit polyclonal, 1:500 for IF), anti-active β1-integrin (mouse monoclonal [12G10], in-house production, 5 µg/ml for IF), anti-inactive β1-integrin (rat monoclonal [Mab13], in-house production, 10 µg/ml for cell culture), and normal IgG2a kappa isotype control (eBioscience, 14-4321-85, rat monoclonal [eBR2a], 10 µg/ml for cell culture).

Secondary antibodies: Alexa Fluor 488/568-conjugated secondary antibodies raised against mouse (Invitrogen, A21202 and A10037, 1:400 for IF) and rabbit (Invitrogen, A21206 and A10042, 1:400 for IF), IRDye 800CW donkey anti-mouse IgG (LI-COR Biosciences, 926-32212, 1:5000 for WB), IRDye 800CW donkey anti-rabbit IgG (LI-COR Biosciences, 926-32213, 1:5000 for WB), and IRDye 680LT donkey anti-mouse IgG (LI-COR Biosciences, 926-68022, 1:5000 for WB).

Validation

All antibodies were used on cells of human origin. The specificity of the β1-integrin-targeting hybridoma antibodies was validated previously using integrin activity-modulating cations: Georgiadou et al. 2017, doi: 10.1083/jcb.201609066. The following phosphorylation-specific antibodies have been validated in previous studies using specific kinase inhibitors: p-FAK (Y397), Alanko et al. 2015, doi: 10.1038/ncb3250; p-ERK1/2 (T202/Y204), Al-Akhrass et al. 2021, doi: 10.1038/s41388-020-01604-5.

Additional validation statements regarding primary antibody reactivity and applications are available on the manufacturers' websites: anti-paxillin, for IF, https://www.bdbiosciences.com/en-us; anti-paxillin, for IF, https://www.scbt.com/home; anti-vinculin, for IF and WB, https://www.sigmaaldrich.com/; anti-talin-1/2, for WB, https://www.novusbio.com/; anti-FAK, for WB, https://www.bdbiosciences.com/en-us; anti-MLC2, for WB, https://www.cellsignal.com/; anti-p-MLC2, for WB, https://www.cellsignal.com/; anti-ERK1/2, for WB, https://www.cellsignal.com/; anti-YAP, for IF, https://www.scbt.com/home; anti-vimentin, for WB, https://www.cellsignal.com/; anti-GAPDH, for WB, https://www.hytest.fi/home/; anti-fibronectin, for IF, https://www.sigmaaldrich.com/.

Eukaryotic cell lines

Policy information about cell lines

Cell line source(s)

U-251MG human glioblastoma cells were obtained from Dr. G. Yancey Gillespie (U. Alabama-Birmingham) (originally from American Type Culture Collection, ATCC). MDA-MB-231 human breast adenocarcinoma cells were purchased from ATCC and U-2 OS human osteosarcoma cells were acquired from German Collection of Microorganisms and Cell Cultures (DSMZ).

Authentication

U-251MG and MDA-MB-231 were authenticated using short tandem repeat assays (at the University of Arizona Genetics Core and DSMZ, respectively). The U-2 OS cells were not authenticated for this study.

Mycoplasma contamination

All cell lines were confirmed negative for mycoplasma on a regular basis.

Commonly misidentified lines
(See ICLAC register)

No commonly misidentified cell lines were used in the study.